

Assessment of thermal, hydraulic, and mechanical constitutive relations on the temperature-induced stress and pore fluid pressure in saturated clays

Mohammadreza Mir Tamizdoust^{a,b}, Omid Ghasemi-Fare^{b,*}

^a Department of Forensic Engineering, Bryant Consultants, Inc., USA

^b Department of Civil and Environmental Engineering, University of Louisville, USA

ARTICLE INFO

Keywords:

THM
Heat transfer
Thermal pressurization
Thermo-elastoplastic deformation
Thermo-osmotic flow

ABSTRACT

Generation and dissipation of temperature-induced pore water pressure can alter the mechanical behavior and characteristics of soil media. Experimental observations indicate that heating/cooling cycles alter the soil fabric which may result in irrecoverable deformations. Previous studies suggest that the contribution of thermo-osmotic (non-Darcian) flow in clays may have a significant role in the thermal pressurization diffusion. Hence, this study aims to investigate the effects of thermal, hydraulic, and mechanical constitutive models such as thermo-plastic deformation along with the thermo-osmotic flow and thermal infiltration on the THM response of clayey soils during heating and cooling phases. It is found that considering temperature-dependent parameters in conjunction with the thermo-poroelastoplastic model improves the results to better capture the thermal pressurization, especially during the cooling phase. Moreover, thermo-elastic deformation majorly affects the thermal pressurization in the heating phase, and thermo-plastic deformation (thermal consolidation) has a major role in stress characteristics close to the heater. The magnitude and sign of thermo-osmotic conductivity strongly depend on the temperature and microstructural properties of clays which cannot be ignored. Comparison of the numerical results with and without considering thermo-osmotic flow and thermal infiltration, confirms the importance of the thermo-osmosis phenomenon during thermal loading in clayey soils.

1. Introduction

Thermal loading can change the hydro-mechanical characteristics of low permeable soils in the vicinity of energy geo-structures, or deep geological repositories, through the expansion of the pore fluid, deformation of pore structure, and soil fabric alterations (Ballarini et al., 2017; Gens et al., 2007; Ghabezloo and Sulem, 2009; Rutqvist et al., 2005; Tamizdoust and Ghasemi-Fare, 2022). An increase in soil temperature may induce expansive or contractive deformations through rearranging of the solid grains, depending on soil stress state (Abuel-Naga et al., 2007b; Baldi et al., 1988; McTigue, 1986). Moreover, thermal loading in an undrained (or weakly drained) condition leads to pore pressure generation also known as thermal pressurization due to the difference in thermal expansion coefficients of pore fluid and the pore volume (Cherati and Ghasemi-Fare, 2021; Delaney, 1982; Ghabezloo and Sulem, 2010; Rice, 2006). Thermal pressurization has been studied in the literature through the thermo-hydro-mechanical (THM) framework (Abed and Sołowski, 2017; Chen et al., 2021a; Cherati and Ghasemi-Fare, 2021; Plúa et al., 2021; Sánchez et al., 2016; Tsang et al.,

2012).

In many numerical studies, the thermo-poroelastic (TPE) constitutive model has been successfully utilized to capture the THM response of saturated and unsaturated soils (Cui et al., 2018; Guayacán-Carrillo et al., 2017; Malekzadeh and Pak, 2009; Tsang et al., 2012; Zhai and Atefi-Monfared, 2020c). In addition, it has been concluded that the coupled interaction between the thermal properties of the saturating fluid and hydro-mechanical properties of the porous medium is significant and needs to be carefully considered (Ghabezloo and Sulem, 2009; Tamizdoust and Ghasemi-Fare, 2020c).

On the other hand, the experimental observations suggest that irreversible deformations may occur during heating and cooling cycles of normally consolidated or slightly overconsolidated clays (Abuel-Naga et al., 2006; Hueckel and Pellegrini, 1992; Joshaghani and Ghasemi-Fare, 2021; Tamizdoust and Ghasemi-Fare, 2020a). Furthermore, the generation and dissipation of thermal pressurization in clayey soils lead to irreversible volumetric contraction which is known as thermal consolidation (Ai and Wang, 2015; Chaudhry et al., 2021; Delage et al., 2000; Joshaghani and Ghasemi-Fare, 2019; Zeinali and Abdelaziz,

* Corresponding author at: 132 Eastern Pkwy, Department of Civil and Environmental Engineering, University of Louisville, Louisville, KY 40207, USA.
E-mail addresses: m.mirtamizdoust@louisville.edu (M.M. Tamizdoust), omid.ghasemifare@louisville.edu (O. Ghasemi-Fare).

2021). This phenomenon is often studied theoretically by considering the thermo-poroelastoplastic (TPEP) constitutive models (Abuel-Naga et al., 2007a; Cui et al., 2000; Hueckel and Borsetto, 1990; Laloui and François, 2009; Sánchez et al., 2005; Sánchez et al., 2012). These constitutive models have been adopted based on the critical state concept by modifying the preconsolidation pressure and the slope of the critical state line at elevated temperatures according to the experimental observations for different clayey soils.

There have been a few studies that considered the TPEP constitutive models to analyze the THM behavior of clays. François et al. (2009) utilized the ACMEG-T model to study the THM process in Boom clay and observed irreversible strains developed close to a heat source. Recently, Abed and Solowski (2017) analyzed the THM behavior of unsaturated Bentonite using the temperature-dependent expansive Barcelona model. However, these studies focused on the effect of temperature on the mechanical response of the medium and neglected the effect of temperature on the mass balance of fluid, such as the osmotic flow and the temperature-dependency of volumetric thermal expansion coefficient of fluid.

In general, fluid flow in clays is not limited to the hydraulic gradient. Chemical, electrical, and thermal gradients may significantly contribute to fluid flow which can be referred to as chemo-osmosis, electro-osmosis, and thermo-osmosis, respectively (Revil, 2017a; Revil and Leroy, 2004; Shackelford et al., 2019; Zhai and Atefi-Monfared, 2020b). Thermo-osmotic flow is a hydraulic constitutive relation that is caused by a thermal gradient and is governed by the thermo-osmotic conductivity. The range of values for the thermo-osmotic conductivity is between 10^{-14} and 10^{-10} $\text{m}^2/\text{C}/\text{s}$ as reported for most clays (Zagorščak et al., 2017); however, some negative values (when fluid flows from cold to warm side) were also measured by Gray (1966). Gonçalves et al. (2012) proposed an upscaled thermo-osmotic permeability coefficient based on physical molecular theory and incorporated it in a macroscale transport equation to investigate the thermo-osmotic flow in natural clays. In their model, the thermo-osmotic permeability is a function of physical and chemical properties of natural clays, such as bulk (equilibrium) salt concentration (c_{eq}), specific surface area (SSA), cation exchange capacity (CEC), and pore space. In a recent study, Chen et al. (2021b) evaluated the thermo-osmosis phenomenon in nanopore structures by utilizing Molecular Dynamics (MD) simulations.

Although recently some researchers have incorporated the thermo-osmotic flow in their theoretical model; however, only constant values of thermo-osmotic conductivity have been considered where the effect of temperature, saturating fluids' salt concentration, and microstructural characteristics of the soil were neglected (Niu et al., 2020; Potts et al., 2021; Zhai and Atefi-Monfared, 2020a; Zhu et al., 2021). As will be shown in this study, changes in such properties can alter the thermo-osmotic conductivity by the order of 100; moreover, they can even change the sign of the thermo-osmotic conductivity in some cases. Hence, careful examination and influence of such parameters should be taken into account for accurate THM modeling. It has been observed in the literature that, thermo-osmotic flux might be relatively lower than Darcian flux for the short term; however, the thermo-osmosis phenomenon can play a significant role in fluid transport in certain applications (e.g., waste repositories) which are designed for the longer-time operation (Shackelford et al., 2019; Tremosa et al., 2012). Sánchez et al. (2010) studied the THM behavior of FEBEX Bentonite as a clay barrier and compared their numerical results with a mock-up test. They concluded that considering thermo-osmotic flow improved the accuracy of their numerical model. Recently, Zagorščak et al. (2017) utilized thermo-osmotic flow to assess the thermal pressurization in Boom clay using a TPE model, and reported that thermo-osmotic flow must be considered to accurately predict the pore water pressure (PWP); however, they used a constant positive value for thermo-osmotic conductivity and also disregarded the effect of other temperature-dependent parameters on thermal pressurization in Boom clay.

The highlight of this study is the incorporation of a thermo-

poroelastoplastic model, thermal infiltration, and the non-Darcian (thermo-osmosis) flow to analyze their impact on the temperature propagation, thermal pressurization, and stress response of a saturated clay. First, we present the complete formulations of balance equations as well as thermal, hydraulic, and mechanical constitutive models. Temperature-dependent properties of the fluid and the medium are also taken into account. Then, we consider multiple models to analyze the effect of different constitutive relations during heating-cooling cycles in Boom clay to understand their effects on the THM process in the saturated condition. The advantages and disadvantages of each model are presented by comparing the simulation results of each modeling approach. In this study, the numerical modeling is handled by COMSOL Multiphysics. Furthermore, the results are compared and validated with observations in the ATLAS III experiment conducted at the underground research facility HADES-URF from April 2007 until November 2009 in Mol, Belgium (Chen et al., 2011; Chen et al., 2017).

2. Theoretical formulation

Macroscopic heat and mass balances, non-Darcian fluid flow, and TPEP constitutive equations are presented in this section. All equations are formulated in Cartesian (x, y, z) coordinate system, where: $\partial(\bullet)/\partial t$, $\nabla(\bullet)$, $\nabla \cdot (\bullet)$, and $\nabla^2(\bullet)$ are time derivative, gradient, divergence, and Laplace of field variables, respectively. Eulerian configuration of the continuum balance and constitutive equations with the assumption of small deformation is considered in this study. Moreover, all constitutive models are expressed in the isotropic condition where the classical soil mechanics sign convention is adopted.

2.1. Macroscopic balance equations

Heat and mass transfer through a saturated deformable soil is governed by solid mass, fluid mass, and energy balances along with the assumption of stress equilibrium in the solid phase. In this study, the saturating fluid is referred to as water. The medium is consisting of mechanically incompressible solid particles with connected pores which are saturated with compressible water. In addition, it is assumed that solid and fluid phases are in local thermal equilibrium since the time associated with the heat transport between phases is very fast in comparison to the other types of transport in the medium. The mass balances of the solid skeleton, fluid (groundwater), and thermal energy are, respectively, defined as (Coussy, 2004):

$$\frac{\partial[(1-n)\rho_s]}{\partial t} + \nabla \cdot [(1-n)\rho_s \mathbf{v}_s] = 0 \quad (1)$$

$$\frac{\partial(n\rho_f)}{\partial t} + \nabla \cdot \mathbf{q}_f = 0 \quad (2)$$

$$\frac{\partial\{[n\rho_f C_f + (1-n)\rho_s C_s]T\}}{\partial t} + \nabla \cdot \mathbf{q}_T = 0 \quad (3)$$

In Eqs. (1)-(3), n (m^3/m^3), ρ_f (kg/m^3), and ρ_s (kg/m^3) are the porosity, water density, and solid density, respectively. T ($^\circ\text{C}$) is the temperature of the medium assigned to all phases. C_f and C_s ($\text{J}/\text{kg}/^\circ\text{C}$) are, respectively, specific heat capacities of the fluid and solid grains. Moreover, \mathbf{v}_s (m/s) is mass-averaged solid velocity vector, \mathbf{q}_f ($\text{kg}/\text{m}^2/\text{s}$) is advective fluid flux, and \mathbf{q}_T (W/m^2) is conductive heat flux. In Eqs. (1) and (2) no mass exchange between solid and fluid phases is considered. In Eq. (3), heat convection is disregarded due to the low permeability of clays.

Porosity variation can be defined through Eq. (1), and by considering mechanically incompressible solid grains. Furthermore, the density of liquid water can vary with temperature and pressure. These state variables are expressed as follows (Coussy, 2004; Ghabezloo and Sulem, 2009):

$$\frac{\partial n}{\partial t} = (1 - n)\nabla \cdot \mathbf{v}_s = (1 - n)\frac{\partial \varepsilon_v}{\partial t} \quad (4)$$

$$\frac{\partial \rho_f}{\partial t} = \rho_f \left[c_f \frac{\partial p_f}{\partial t} - \alpha_f \frac{\partial T}{\partial t} \right] \quad (5)$$

In Eq. (4), ε_v (m/m) is the volumetric strain which is the summation of mechanical and thermal strains. In the TPEP constitutive model, ε_v can be decomposed to elastic, thermal, and plastic deformations. In Eq. (5), p_f (Pa) indicates pore fluid pressure, c_f (1/Pa) is the compressibility coefficient, and α_f (1/°C) is the linear thermal expansion coefficient of the water. By combining Eqs. (2), (4), and (5), we have:

$$nc_f \rho_f \frac{\partial p_f}{\partial t} + \nabla \cdot \mathbf{q}_f = \rho_f \left[n \alpha_f \frac{\partial T}{\partial t} - (1 - n) \frac{\partial \varepsilon_v}{\partial t} \right] \quad (6)$$

The right-hand side of Eq. (6) is related to the influence of volumetric deformation (or porosity change) and thermal variations (e.g., thermal expansion of fluid) in the porous medium on the thermal pressurization. It has been shown in previous research that even a small perturbation in porosity can greatly affect thermal pressurization (Tamizdoust and Ghasemi-Fare, 2019, 2020b). Pore fluid pressure and temperature are calculated by solving Eqs. (3) and (6). Mechanical, hydraulic, and thermal constitutive relations should be specified to determine ε_v , \mathbf{q}_f , and \mathbf{q}_T , respectively.

2.2. Mechanical equilibrium

Soil stress equilibrium is expressed as (Coussy, 2004):

$$\nabla \cdot \boldsymbol{\sigma} + [n\rho_f + (1 - n)\rho_s] \mathbf{g} = 0 \quad (7)$$

In the framework of soil poromechanics, total Cauchy stress, $\boldsymbol{\sigma} = \boldsymbol{\sigma}' + p_f \mathbf{I}$ (N/m²), is decomposed to the Terzaghi's effective stress, $\boldsymbol{\sigma}'$ (N/m²), and pore fluid pressure, p_f . \mathbf{I} is the identity second-order tensor. It should be noted that effective stress is related to the deformation of porous media through a mechanical constitutive model. \mathbf{g} (m/s²) is the acceleration of the gravity vector.

2.3. Thermo-poroelastoplastic Constitutive Model

In this study, in addition to the elastic strain, thermally-induced plastic strains have been considered to evaluate the interaction between thermoplastic deformation and thermal pressurization. To consider the thermoplastic deformations, the TPEP constitutive model, similar to ACMEG-T (Laloui and François, 2009), is implemented in the model developed in COMSOL Multiphysics to analyze the THM process in clays. According to the small deformation theory of plasticity, the total mechanical strain increment can be additively decomposed to elastic, thermal, and plastic parts:

$$\dot{\boldsymbol{\varepsilon}} = \dot{\boldsymbol{\varepsilon}}^e + \dot{\boldsymbol{\varepsilon}}^t + \dot{\boldsymbol{\varepsilon}}^p \quad (8)$$

where $\dot{\boldsymbol{\varepsilon}}^e$ is the elastic strain rate, $\dot{\boldsymbol{\varepsilon}}^t$ is the thermal strain rate, and $\dot{\boldsymbol{\varepsilon}}^p$ is the plastic strain rate. Following the theory of linear thermo-elasticity, the elastic and thermal strain rates are defined as:

$$\dot{\boldsymbol{\varepsilon}}^e = \mathbb{C}^e : \dot{\boldsymbol{\sigma}} \quad (9)$$

$$\dot{\boldsymbol{\varepsilon}}^t = -\boldsymbol{\alpha}_d \dot{T} \quad (10)$$

where $\boldsymbol{\alpha}_d$ (1/°C) is drained linear thermal expansion coefficient tensor of the porous medium and can be expressed as $\boldsymbol{\alpha}_d = \alpha_d \mathbf{I}$ considering isotropic thermal expansion coefficient. The negative sign in Eq. (10) represents the dilative deformation. It is to be noted that the drained linear thermal expansion coefficient is assumed to be equal to the linear thermal expansion coefficient of solid grains (α_s). Moreover, \mathbb{C}^e (Pa) is the compliance elasticity 4th order tensor and is a function of Poisson's ratio, ν (-) and Young's modulus, E (Pa), which is defined as (Modaressi

and Laloui, 1997):

$$E = E_{ref} \left(\frac{p'}{p'_{ref}} \right)^m \quad (11)$$

E_{ref} (Pa) is the reference Young's modulus, $p' = -I_1/3$ is the mean effective stress, I_1 (Pa) is the first invariant of the stress tensor, p'_{ref} (Pa) is the reference pressure, and m (-) is a constant value. Eqs. (9)-(11) govern the TPE constitutive model.

According to the multi-mechanism concept, the increment of plastic strain can be expressed as (Laloui and François, 2009):

$$\dot{\boldsymbol{\varepsilon}}^p = \sum_{i=1}^2 \lambda_i^p \frac{\partial Q_i}{\partial \boldsymbol{\sigma}} \quad (12)$$

Q (Pa) and λ^p (-) are, respectively, plastic potential function and plastic multiplier for different yielding mechanisms. Upon yielding, the plastic multiplier is a positive value, otherwise, it is zero. In Eq. (12), the increment of plastic strain is proportional to the direction of the gradient of plastic potential according to the conventional plastic flow rule. However, in the case of loading conditions with the rotation principal stresses, the tangential plastic flow rule must also be considered (Veiskarami and Tamizdoust, 2017). In this study, the plastic potential is assumed to be equal to the yield surface (f) considering the associated plastic flow rule ($Q = f$). ACMEG-T model which is adopted in this study consists of two yield surfaces in which they govern the isotropic (f_{iso}) and deviatoric (f_{dev}) thermoplastic mechanisms. With a slight modification from the ACMEG-T model, we considered modified Cam Clay yield surface for the deviatoric part of the yield function:

$$f_{iso} = p' - p'_{cT} r_{iso}; f_{dev} = \frac{q^2}{p'} + M_T^2 (p' - p'_{cT}) r_{dev} = 0 \quad (13)$$

In Eq. (13), $q = \sqrt{3J_2}$ is the deviatoric stress, J_2 (Pa²) is the second invariant of the deviatoric stress tensor, p'_{cT} (Pa) and M_T (-) are the temperature-dependent preconsolidation pressure and slope of the critical state line. r_{iso} and r_{dev} are, respectively, the degree of plastification (mobilized hardening) of isotropic and deviatoric yield limits. These two parameters facilitate the loading-unloading stress-strain evolution. The idea of the plastification parameter is conceptualized in bounding surface theory which states that plastic deformation may occur when the stress state is on or within the bounding surface (e.g. external surface) (Dafalias, 1981). r_{iso} and r_{dev} are defined as (Laloui and François, 2009):

$$r_{iso} = r_{iso}^e + \frac{\varepsilon_{iso,vol}^p}{a_{iso} + \varepsilon_{iso,vol}^p} \quad (14)$$

$$r_{dev} = r_{dev}^e + \frac{\varepsilon_{dev}^p}{b_{dev} + \varepsilon_{dev}^p} \quad (15)$$

In Eqs. (14) and (15), r_{iso}^e and r_{dev}^e are elastic nuclei of isotropic and deviatoric mechanisms, respectively; a_{iso} and b_{dev} are material parameters, $\varepsilon_{iso,vol}^p$ is the volumetric plastic strain for the isotropic yielding mechanism and, ε_{dev}^p is the deviatoric plastic strain.

Non-isothermal experimental observations on clays determined that preconsolidation pressure and slope of the critical state line are strongly temperature-dependent (Hueckel et al., 2011); therefore, pre-consolidation pressure can be defined as follows (Laloui and Cekerevac, 2003):

$$p'_{cT} = p'_{cT_0} \left[1 - \gamma_T \log \left(1 + \frac{T}{T_0} \right) \right] \exp(\beta \varepsilon_{vol}^p) \quad (16)$$

where p'_{cT_0} (Pa) is the preconsolidation pressure at reference temperature (T_0), and γ_T (-) is a material parameter. In Eq. (16), $\exp(\beta \varepsilon_{vol}^p)$ governs the isotropic hardening behavior of soil where β (-) is the plastic compressibility modulus and ε_{vol}^p (m/m) is the volumetric plastic strain. Moreover, the temperature-dependent slope of the critical state line is predicted as (Laloui, 1993):

$$M_T = \frac{6 \sin \phi'_0}{3 - \sin \phi'_0} - g_T(T - T_0) \quad (17)$$

ϕ'_0 (deg) is the friction angle at the reference temperature and g_T (1/°C) is an average slope of variation of friction angle at critical state with temperature. Eqs. (9)-(17) complete the TPEP constitutive model used in this study. The volumetric parts of Eqs. (9), (10), and (12) are used to calculate the porosity change in Eq. (4).

2.4. Hydraulic and Thermal Constitutive Models

The fluid flow in soils is often governed by Darcy's law; however, in clayey soils, special attention has been given to non-Darcian flow governed by osmosis phenomena (Gonçalvès et al., 2004). Moreover, the conductive heat flux in this study is comprised of Fourier's law of thermal conduction and thermal infiltration due to the mechano-caloric effect (Gonçalvès and Trémosa, 2010). Thermo-osmosis and thermal infiltration are conjugated fluxes based on the Onsager reciprocity principle. In this study, we follow the macroscopic (upscaled) fluid and thermal fluxes proposed by Gonçalvès and Trémosa (2010) and Gonçalvès et al. (2012):

$$\mathbf{q}_f = -\rho_f \left[\underbrace{\frac{k}{\mu} (\nabla p_f + g_z)}_{\text{Darcy's flow}} + \underbrace{\frac{k_T}{\mu} \nabla T}_{\text{Thermo-osmosis flow}} \right] \quad (18)$$

$$C_{HB} = \underbrace{\sum_i N_w^i \bar{C}_i}_{\text{concentration of HB of pore water molecules in the first shell of hydrated ions}} \frac{1}{2N_{HB}^i} + \underbrace{\left(\bar{C}_w - \sum_i N_w^i \bar{C}_i \right)}_{\text{concentration of HB of pore water molecules not affected by the ions}} \left(\frac{b - b_s}{b} N_{HB}^b + \frac{b_s}{b} N_{HB}^s \right) \frac{1}{2} \quad (22)$$

$$\mathbf{q}_T = - \left\{ \underbrace{\frac{k_p}{\mu} \nabla p_f}_{\text{Thermal infiltration}} + \underbrace{[n\lambda_f + (1-n)\lambda_s] \nabla T}_{\text{Fourier's law of conduction}} \right\} \quad (19)$$

In Eq. (18), k (m²) is the isotropic intrinsic permeability of the medium, μ (Pa.s) is the dynamic viscosity of the fluid, and k_T (Pa.m/°C) is thermo-osmotic permeability (k_T/μ is the thermo-osmotic conductivity). In Eq. (19), λ_f and λ_s (W/m/°C) are the thermal conductivities of the fluid and solid grains, and k_p (m²/s) is the thermal-infiltration coefficient. A permanent negative charge that exists on the clay particle surface is counterbalanced by the accumulated ions (i.e. counterions and generally positive) of adsorbed pore fluid in Stern and Diffuse layers (Gonçalvès and Trémosa, 2010; Revil and Leroy, 2004). The thickness of the diffuse layer can be in the order of nanometers which is the same as the micropores in clay materials. The overlapping of the adjacent diffuse layers of clay minerals manifests the presence of an electrical field which contributes to the alteration of adsorbed fluid structure in terms of its hydrogen bond (HB) network (Gonçalvès and Trémosa, 2010). The

alteration of hydrogen bonds results in changing of specific enthalpy of adsorbed fluid in comparison to the bulk fluid (Gonçalvès et al., 2012; Gonçalvès and Trémosa, 2010; Revil and Leroy, 2004; Roshan et al., 2015). By incorporating the difference of adsorbed and bulk specific enthalpy, Gonçalvès and Trémosa (2010) defined the thermo-osmotic permeability and thermal-infiltration coefficient as follows:

$$k_T = \frac{k\Delta H}{T}; k_p = k\Delta H \quad (20)$$

where ΔH (J/m³) is the macroscopic excess specific enthalpy due to fluid-solid interactions in which $\Delta H > 0$ implies the fluid flow from hot to cold region. Derjaguin and Sidorenkov (1941) provided a theoretical formulation for ΔH by utilizing the HB modification (Derjaguin and Sidorenkov, 1941; Gonçalvès et al., 2012):

$$\Delta H = (C_{HB}^b - C_{HB})\Delta H_{HB} \quad (21)$$

C_{HB}^b (mol/m³) and C_{HB} (mol/m³) are the HB concentrations in the bulk and pore fluid and ΔH_{HB} (kJ/mol) is the energy needed to break one mole of HB. As recommended by Gonçalvès et al. (2012), $\Delta H_{HB} \approx 14.5$ kJ/mol is considered in this study. Detailed calculations of ΔH which are adopted in the current numerical model to predict the variations of the thermo-osmotic permeability (k_T) during the thermal loading are presented by Gonçalvès et al. (2012) and Revil (2017b) in detail. Please note, in contrast to available literature for THM analysis in clays that considered the thermo-osmosis phenomenon, the thermo-osmotic permeability is not a constant value.

$$C_{HB}^b = \underbrace{c_{eq} \sum_i N_w^i}_{\text{concentration of HB of bulk water molecules in the first shell of hydrated salinity}} \frac{1}{2N_{HB}^i} + \underbrace{\left(C_w - c_{eq} \sum_i N_w^i \right)}_{\text{concentration of HB of bulk water molecules not affected by salinity}} \frac{1}{2N_{HB}^b} \quad (23)$$

In Eqs. (22) and (23), the bar sign represents the pore fluid properties to differentiate them from bulk fluid ones. i is the summation dummy index which indicates cation (+) and anion (-). N_w^i is the number of water molecules in the first hydration shell of the cation and the anion ($N_w^+ = N_w^- = 6$). N_{HB}^i is the mean number of HB per water molecule in the first hydration shells ($N_{HB}^+ = 2.27$; $N_{HB}^- = 2.65$). N_{HB}^b and N_{HB}^s are mean numbers of HB per water molecule of bulk and highly ordered water, respectively ($N_{HB}^b = 3.5$; $N_{HB}^s = 3.75$). b_s and b are the mean half-pore size and the half-thickness of highly ordered water, respectively (m). ($b_s = 1$ nm). In the same order, \bar{C}_w and \bar{C}_i (mol/m³) are water and ions concentrations in the pore space. C_w and c_{eq} (mol/m³) are water and salt

concentrations in the bulk fluid. Moreover, the mean half-pore size can be calculated as (Gonçalvès et al., 2012):

$$b = \frac{n}{(1-n)\rho_s SSA} \quad (24)$$

where SSA (m^2/kg) is the external specific area of the porous medium.

There are four unknowns in Eqs. (21) and (22) i.e., \overline{C}_w , \overline{C}_+ , \overline{C}_- , and C_w which need to be determined. The concentration in the electrical double layer (EDL) in the vicinity of clay surface (\overline{C}_+ and \overline{C}_-) can be obtained by solving Poisson-Boltzmann (PB) equation in the finite distance (2b) between two clay particles. In small pores and low concentrations of salt (<0.1 M [=mol/l]), EDL parallel particles overlap. PB equation in this case should be solved numerically. However, some analytical solutions for PB are available for low surface potential (often less than $\psi = 50$ mV). An alternative approach to solving the PB equation is using Donnan Equilibrium where an average of charge density can be obtained. The advantage of using Donnan equilibrium is the fact that it can be used in the Representative Element Volume (REV) scale and is simple to incorporate in continuum models. Here, by following the approach of Revil (2017b), we can obtain the ionic concentration in pore water for the case of 1:1 salt solution such as NaCl:

$$\overline{C}_{\pm} = c_{eq} \left(\sqrt{1 + \Theta^2} \pm \Theta \right) \quad (25)$$

where Θ is a dimensionless number:

$$\Theta = \frac{Q_V}{2eN_a c_{eq}} \quad (26)$$

e is the elementary charge (1.6×10^{-19} C), N_a is Avogadro's constant (6.02×10^{23} 1/mol). Furthermore, the volumetric charge density (Q_V [C/m^3]) is defined as:

$$Q_V = \frac{(1-n)CEC\rho_s}{n} \quad (27)$$

In Eq. (27), CEC (C/kg) is the cation exchange capacity. Note that for practical purposes, CEC is usually expressed in meq/g (1 meq/g = 96320 C/kg). Finally, we use the following conservation equation for bulk and pore fluid concentrations to solve for \overline{C}_w and C_w (Revil, 2017b):

$$\Omega_w \overline{C}_w + \sum_i \Omega_i \overline{C}_i = 1 \quad (28)$$

$$\Omega_w C_w + c_{eq} \sum_i \Omega_i = 1 \quad (29)$$

Ω_w and Ω_i are molar volumes of the water and ions, respectively ($m^3/$

mol). ($\Omega_w=23.8 \times 10^{-6}$, $\Omega_+=17.4 \times 10^{-6}$, and $\Omega_- = 18.0 \times 10^{-6}$). According to the equations presented above, HB concentration is a function of fluid salinity, pore size, porosity, density, cations exchange capacity, and specific surface area of the solid.

2.5. Thermal properties of water

Despite the availability of many theoretical and numerical studies on THM analysis on soils, there are only a few studies that carefully considered the effect of temperature-dependent properties of the saturating fluid on the THM process in soil media (Braun et al., 2021b; Tamizdoust and Ghasemi-Fare, 2020c). Therefore, a rigorous numerical framework is needed to compare different aspects of temperature changes and mechanical deformation on THM behavior of clayey soils while thermo-osmosis phenomenon, thermal infiltration, and thermo-plastic deformations, and real-time properties of soil and saturating fluid are considered. Fig. 1(a) and (b) illustrate the thermodynamic properties of water for the temperature ranging from 0 to 100 °C which are calculated based on the formulations provided by the International Association for the Properties of Water and Steam (IAPWS) (Spang, 2002).

All equations presented in this section are adopted in COMSOL Multiphysics to assess and compare different thermal, hydraulic, and mechanical properties of the porous media on the THM behavior of clays.

3. Results and discussion

3.1. ATLAS III Experiment

Boom clay is a natural deposit of over-consolidated clay ($OCR = 2.4$) which has been considered as a suitable porous environment for deep geological repositories in Belgium (Mertens et al., 2004). Therefore, different experiments have been performed in underground research laboratories to experimentally investigate the THM response of the Boom clay at elevated temperatures. In this study, the numerical results are compared with the ATLAS III experiment that was conducted in HADES underground research facility (started in 2007). One of the most important objectives of the ATLAS III experiment was to obtain more accurate temperature and pore water pressure (PWP) evolutions around a horizontal heat source at a large scale in comparison to the first ATLAS experiment that was conducted in the 1990s.

ATLAS III consists of a horizontal main borehole (19 m long with an external diameter of 190 mm and an internal diameter of 160 mm) where the heaters cover a section of the main borehole (from 11 to 19 m). AT85E, AT93E, and AT98E are observation boreholes that are

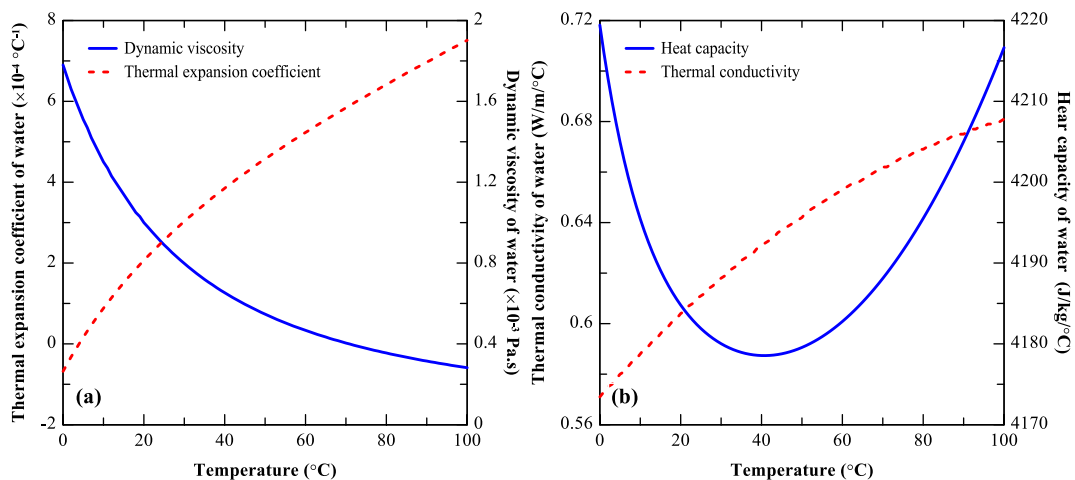


Fig. 1. Thermodynamic properties of bulk water for different temperatures at atmospheric pressure (Spang, 2002): (a) Thermal expansion coefficient and dynamic and viscosity, and (b) heat capacity and thermal conductivity.

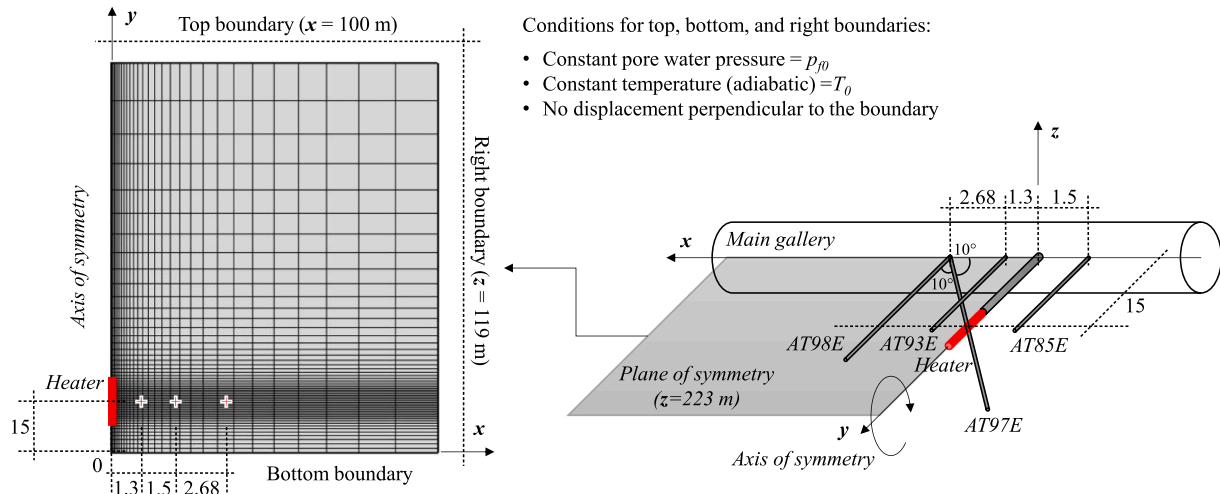


Fig. 2. The schematic representation of the ATLAS III experiment and the numerical domain.

- Conditions for top, bottom, and right boundaries:
- Constant pore water pressure = p_{f0}
 - Constant temperature (adiabatic) = T_0
 - No displacement perpendicular to the boundary

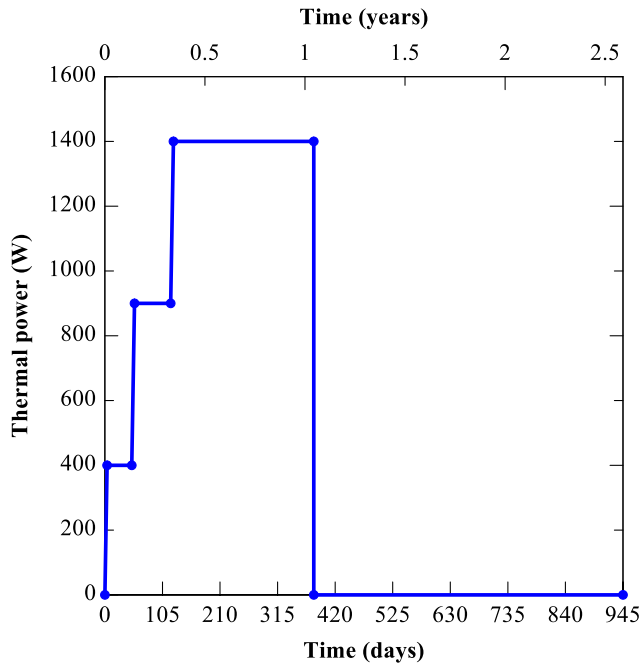


Fig. 3. Thermal power of the heater in ATLAS III experiment.

Table 2

Parameters used in TPEP and TPE constitutive models.

Parameters	Values	Units	References
ν	0.125	-	Chen et al. (2011)
E_{ref}	700	MPa	Chen et al. (2011); Schuster et al. (2001)
m	0.4	-	François et al. (2009)
$*e_0$ (Initial void ratio)	0.639	m^3/m^3	Bernier et al. (2007)
$*\lambda$ (Critical state parameter)	0.122	-	Baldi et al. (1987)
$*\kappa$ (Critical state parameter)	0.031	-	
p'_{cT0}	6	MPa	François et al. (2009)
p'_{ref}	2.25	MPa	
ϕ'_0	16	Deg	
γ_T	0.55	-	
g_T	0.0085	$1/^\circ C$	
r_{iso}^e	0.415	-	
r_{dev}^e	0.3	-	
a_{iso}	0.014	-	
b_{dev}	0.007	-	

* $\beta = (1 + e_0) / (\lambda - \kappa) = 18$.

located at 1.5, 1.3, and 2.86 m, respectively, away from the main borehole in the horizontal plane (xy). Finally, the AT97E borehole (95 mm in diameter) is constructed with 10° inclination towards the main borehole with a 10° downward inclination passing underneath the main borehole. The schematic overview of the ATLAS III experiment is illustrated in Fig. 2. More information about this experiment is given by Chen et al. (2011). The experimental observation provides the means to numerically simulate the THM process and study the thermo-osmosis phenomenon and thermal infiltration while considering thermoplastic deformations in clays at a large-scale well-controlled experiment.

Thermal loading for ATLAS III consists of multiple steps of heating and cooling (Chen et al., 2011). Fig. 3 depicts the thermal power at the heater during different stages of the experiment which is also used in the current study.

3.2. Thermo-hydro-mechanical properties of boom clay

The mechanical, hydraulic, and thermal properties of Boom clay are presented in Table 1. There are some uncertainties associated with the values of SSA and c_{eq} for Boom clay. For example, SSA is reported to be 44 and $150 m^2/g$ in different studies (Al-Mukhtar et al., 1996; Gonçalves et al., 2012). Furthermore, there is not much available data for the salt concentration of the saturating fluid of in-situ Boom clay. Hence, we

Table 1

Physical properties of Boom clay.

Parameters	Values	Units	References
ρ_{f0}	1000	kg/m^3	François et al. (2009)
ρ_s	2670	kg/m^3	
n_0	0.39	m^3/m^3	Bernier et al. (2007)
$*k_0$	2.5×10^{-19}	m^2	
c_f	4.5×10^{-10}	$1/Pa$	Spang (2002)
C_s	730	$J/kg/^\circ C$	(Chen et al., 2017)
λ_s	1.65	$W/m/^\circ C$	Chalindar et al. (2010)
α_s	1.3×10^{-5}	$1/^\circ C$	Baldi et al. (1991)
CEC	0.082	meq/g	Gonçalvès et al. (2012)
b	5.44	nm	

* Intrinsic permeability is calculated based on the Kozeny-Carman equation: $k = k_0[(1 - n_0)/(1 - n)]^2(n/n_0)^3$.

Table 3
Numerical models considered in this study.

	Model 1	Model 2	Model 3	Model 4	Model 5
Mechanical	TPE ($E = E_{ref}$)	TPE (E from Eq. (11))	TPEP (E from Eq. (11))	TPE (E from Eq. (11))	TPEP (E from Eq. (11))
Hydraulic	$k_T = 0$ $\alpha_f = 3.5 \times 10^{-4} 1/^\circ\text{C}$ $\mu = 0.001$ Pa.s	$k_T = 0$ $\alpha_f = \alpha_f(T)$ $\mu = \mu(T)$	$k_T = 0$ $\alpha_f = \alpha_f(T)$ $\mu = \mu(T)$	k_T from Eq. (20) $\alpha_f = \alpha_f(T)$ $\mu = \mu(T)$	k_T from Eq. (20) $\alpha_f = \alpha_f(T)$ $\mu = \mu(T)$
Thermal	$k_p = 0$ $\lambda_f = 0.59$ W/m/ $^\circ\text{C}$ $C_f = 4200$ J/kg/ $^\circ\text{C}$	$k_p = 0$ $\lambda_f = \lambda_f(T)$ $C_f = C_f(T)$	$k_p = 0$ $\lambda_f = \lambda_f(T)$ $C_f = C_f(T)$	k_p from Eq. (20) $\lambda_f = \lambda_f(T)$ $C_f = C_f(T)$	k_p from Eq. (20) $\lambda_f = \lambda_f(T)$ $C_f = C_f(T)$

perform an additional parametric study to better illustrate the impact of these parameters on thermo-osmotic conductivity. The remaining parameters in Table 1 for Boom clay are adopted from Gonçalves et al. (2012).

Table 2 presents the calibrated parameters adopted in the Finite

Element (FE) numerical scheme. The calibrated parameters are adopted from François et al. (2009), Chen et al. (2011), and Schuster et al. (2001).

3.3. Numerical models for the ATLAS III Experiment

In the main part of this study, we consider 5 models for different assumptions to systematically analyze the effect of different parameters/constitutive relations. In model 1, the TPE model is used with constant temperature-independent properties of fluid and mechanical properties of the medium. Model 2 is also based on the TPE assumption while considering temperature and stress-dependent properties of the fluid and the strength parameters of the soil. In model 3, in addition to variable fluid and soil properties, we consider the thermo-plastic deformation as well. Models 4 and 5, respectively, are based on the same assumptions we consider in models 2 and 3, while we utilize the thermo-osmosis and thermal infiltration fluxes in these models (models 4, and 5). The details of the numerical models are expressed in Table 3.

3.4. Numerical simulations

The governing balance equations along with TPE and TPEP constitutive models are implemented in COMSOL Multiphysics v5.3a which is based on the finite element method to simulate the ATLAS III experiment. A 2D axisymmetric domain around the horizontal plane (xy) is

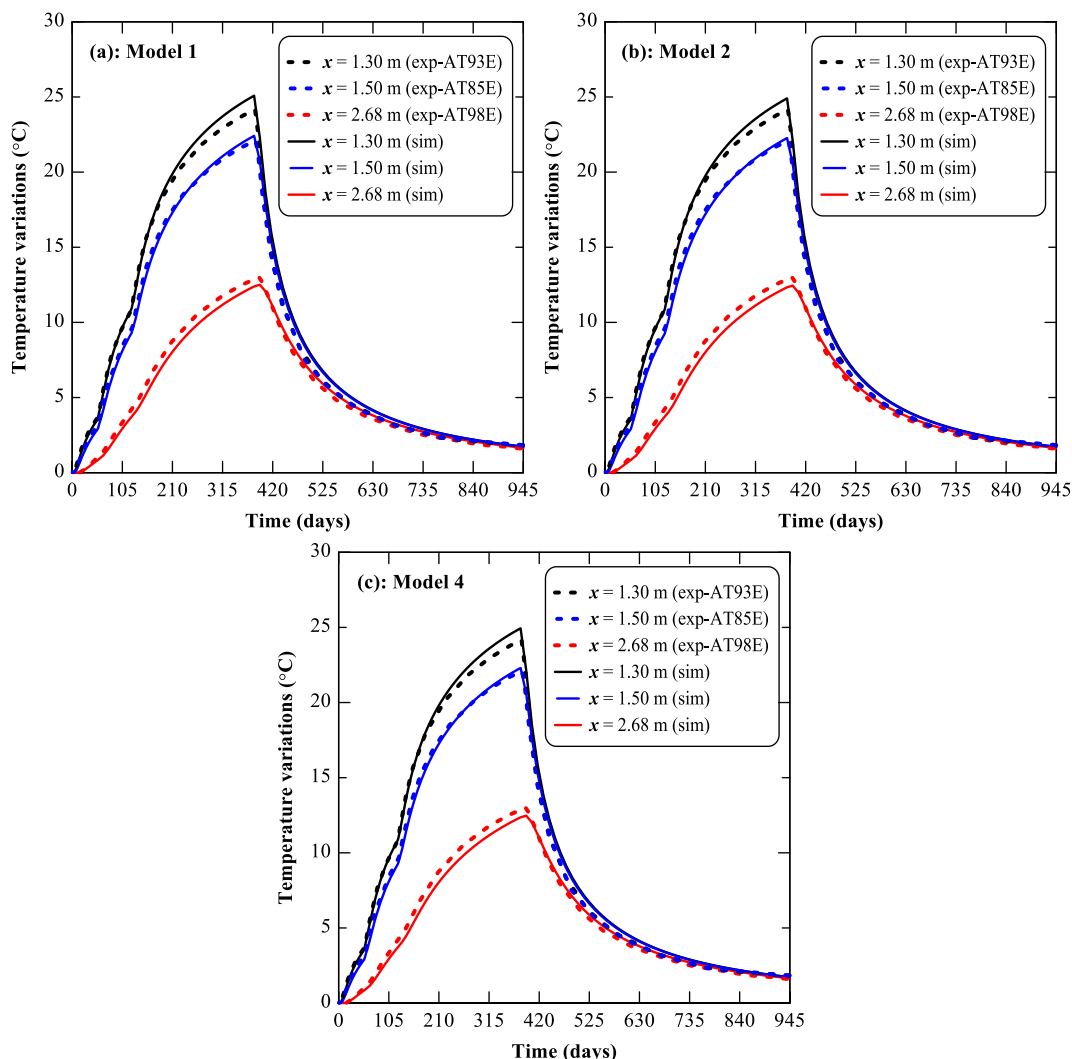


Fig. 4. Temperature evolution against time at $x = 1.3, 1.5,$ and 2.68 m from the heat source: (a) Model 1, (b) model 2, and (c) model 4.

considered where the heat source is placed at the symmetry boundary. A rectangular domain with 100 m in perpendicular (x-direction) and 119 m in parallel (y-direction) direction to the heat source is accounted to minimize the effect of boundary conditions on the results. The in-situ initial conditions adopted in the FE model are as follows (Bernier et al., 2007; François et al., 2009): $\sigma_x = \sigma_y = \sigma_z = 4.5$ MPa, $p_f = 2.25$ MPa, and $T_0 = 16.5$ °C. Constant temperature and pore water pressure equal to the initial values are considered for all boundaries except at the axisymmetric axis. The perpendicular displacement to the boundaries is prevented. The schematic representation of the numerical domain and boundary conditions are illustrated in Fig. 2. After a series of mesh sensitivity analyses, the domain is discretized with 1770 rectangular quadratic finite elements.

The structural, subsurface flow, and heat transfer modules available in COMSOL Multiphysics are modified to implement the governing partial differential equations (PDEs) presented in the previous section. The PDE equations are implicitly solved using the PARDISO direct matrix solver which is available in the COMSOL Multiphysics software. The backward Euler method is employed for time advancement.

3.5. Interpretation of the results

Temperature, thermal pressurization, and averaged total stress during the heating/cooling phases of the experiment are compared with the numerical results.

3.5.1. Temperature variations

Comparison of the numerical results obtained from models 1, 2, and 4 and experimental observations are shown in Fig. 4(a), (b), and (c), respectively. The measurement points are aligned with the center of the heater ($y = 15$ m). The numerical models predict the temperature variations with good accuracy for different distances from the heater. Results obtained by all the modeling approaches are almost the same. It is interesting to note that the temperature variations with time can also be predicted accurately without considering the thermal infiltration phenomenon or temperature dependency of thermal properties. Therefore, the mechano-caloric effect on heat transfer is negligible in the current case. This observation was expected since, the conduction mechanism is more significant compares to other heat transfer mechanisms (e.g., convective heat transfer through thermo-osmotic flow) in clayey soils. Furthermore, plastic deformation also has a negligible effect on temperature evolution (not shown).

3.5.2. Thermal pressurization (Models 1, 2, and 3)

Fig. 5(a), (b), and (c) show the comparison of thermal pressurization ($p_f - p_{f0}$) observed at the measurement borehole during the heating/cooling cycles with numerical models 1–3. These three models are considered to explore the effects of different thermal, hydraulic, and mechanical properties of the porous medium and the saturated fluid on thermal pressurization. Note, the constant thermal expansion coefficient of fluid has been mostly used in THM modeling studies (Chen et al.,

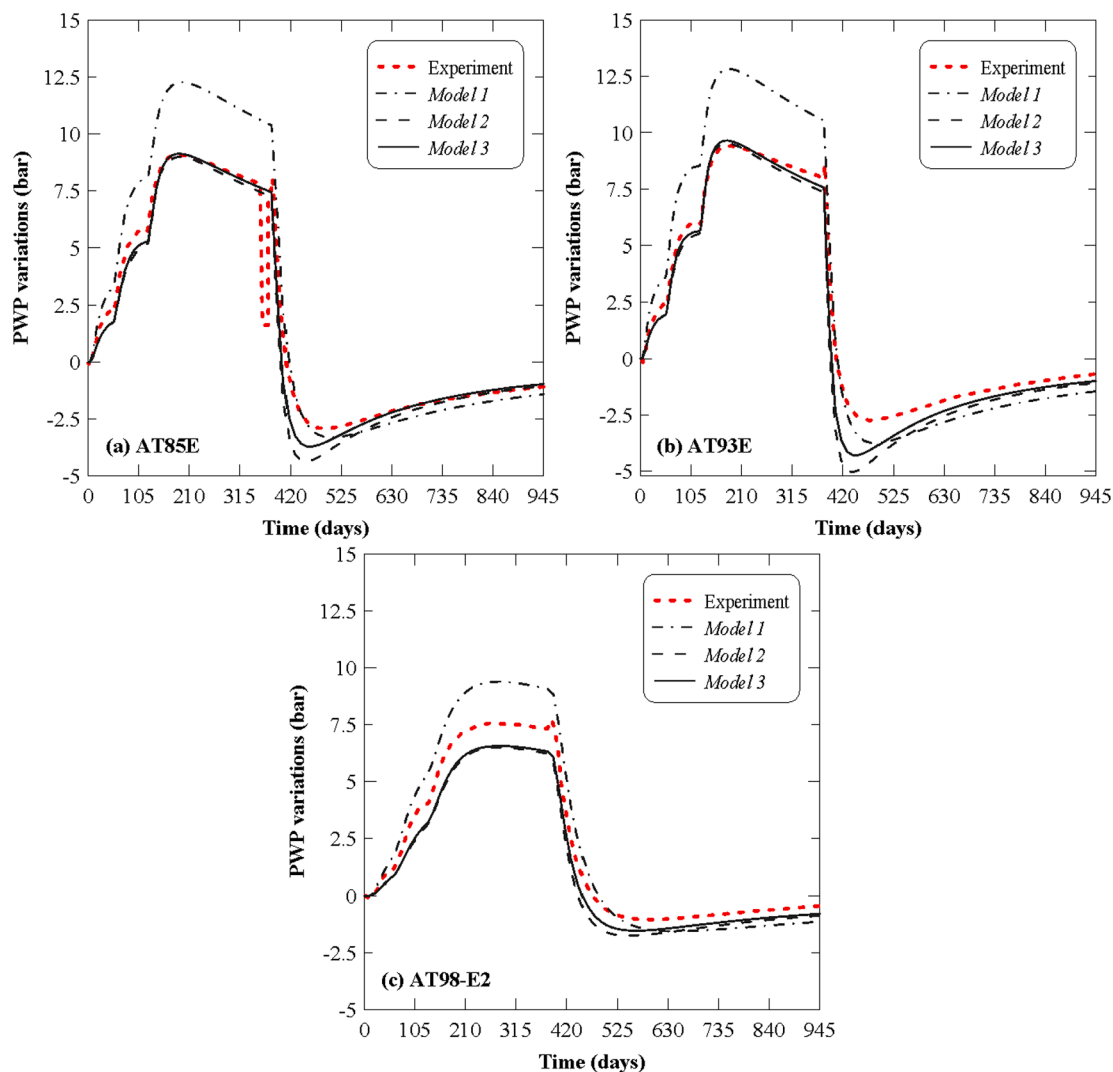


Fig. 5. Thermal pressurization against time by utilizing model 1, 2, and 3: (a) $x = 1.5$ m, (b) $x = 1.3$ m, and (c) $x = 2.68$ m from the heat source.

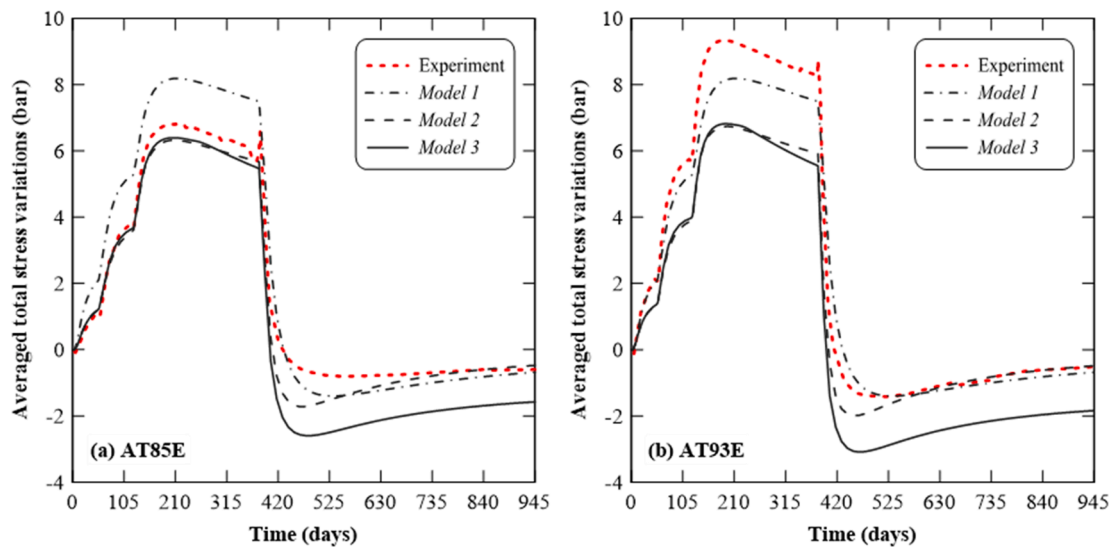


Fig. 6. Averaged total stress variations against time by utilizing model 1, 2, and 3: (a) $x = 1.5$ m and (b) $x = 1.3$ m from the heat source.

2017; Hueckel et al., 2011). By comparing the results in Fig. 5(a), (b), and (c), it is evident that the model with variable α_f (Models 2 and 3) predicts thermal pressurization more accurately compared to the model with constant α_f (Model 1). Indeed, the thermal expansion coefficient of water increases more than 700% at a temperature of 100 °C and higher compares to the initial 16.5 °C temperature (see Fig. 1(a)). The difference in the thermal pressurization predicted by TPE (Model 2) and TPEP (Model 3) approaches is noticeable at the beginning of the cooling phase. The TPE model estimates higher pressure variation than the TPEP model. This is due to the irrecoverable (plastic) deformation (thermal consolidation) that happens in the vicinity of the heat source during the cooling phase at which excess pore water pressure dissipates. However, during heating phases, the difference in numerical results obtained from TPE and TPEP models is less noticeable, since the thermo-elastic deformation is dominant compared to the thermal plastic deformation.

3.5.3. Total stress variations (Models 1, 2, and 3)

The variations of averaged total stress obtained from models 1, 2, and 3 are presented in Fig. 6(a) and (b) and compared with the experimental observations. According to Chen et al. (2011), there are four flat jacks at the left, top, right, and bottom sides of the instrumentation tubing for each measurement borehole. The averaged values of all these measurements are shown in Fig. 6(a) and (b). In Fig. 6(a), model 1 overestimates the total stress variation during heating phases. In contrast, during the same period, models 2 and 3 predict the total stress variation with better accuracy. In the cooling phase, models 1 and 2 show somewhat similar results. This happens because during the cooling phase, soil's temperature drops and reaches almost initial temperature in which the constant and temperature-dependent values of thermal expansion coefficient and viscosity of water (which are responsible for the fluid expansion and the PWP diffusion) are almost equal for these two models. Model 3 (TPEP model), however, yields higher stress variation than models 1 and 2 that is because of the amount of irrecoverable deformation obtained by the ACMEG-T constitutive model. Due to the thermal history of Boom clay, the accumulated plastic strain during heating phases irreversibly affects the stress characteristics of the soil surrounding the heater. That is why, during the cooling phase, the results of TPE and TPEP models noticeably deviate from one to another. Should a different heating/cooling cycle be imposed, a different thermo-plastic behavior could be expected. Model 3 underestimates the stress variation in the cooling phase. Different thermo-elastoplastic constitutive models have been used to evaluate the thermo-plastic behavior of Boom clay (Chen et al., 2011; Cui et al., 2000).

Nonetheless, a more detailed comparison between different thermo-plastic constitutive models is required to shed more light on the thermo-plastic deformation and subsequently on the total stress response of Boom clay to evaluate their performance when it is subjected to elevated temperature. The simulation results of all 3 models follow the same trend for the AT93E borehole depicted in Fig. 6(b). The predictions underestimate the total stress variations obtained from experimental data in the heating phase.

3.5.4. Parametric study of thermo-osmotic conductivity

In the following, we focus on the effect of thermo-osmotic flow and thermal infiltration on the thermal pressurization and total stress variations in the vicinity of the heater. Fig. 7(a) and (b) present the influence of c_{eq} and SSA on the thermo-osmotic conductivity (k_T/μ), respectively, at different temperatures. Fig. 7(a) and (b) indicate that absolute value of k_T/μ increases with temperature regardless of the concentration and surface area because the viscosity of water decreases with temperature; however, the rate and magnitude of this increase depend on the concentration and surface area. Moreover, $c_{eq} = 10^{-7}$ M and 10^{-2} M are bulk ion concentrations of distilled water and water (Gonçalvès et al., 2012) which are compared with higher concentrations in Fig. 7(a) that can exist in the field. It is interesting to mention that the increase in bulk concentration changes the sign of k_T from positive to negative which, consequently, changes the direction of thermo-osmosis flow. Fig. 7(b) illustrates that by increasing SSA from 44 to 150 m²/g, thermo-osmotic conductivity changes from positive to negative values regardless of the bulk concentration. Fig. 7(c)–(e) indicate the changes in thermally induced pore water pressure with or without considering the thermo-osmosis effect. Fig. 7(c) and (d) show the thermal pressurization versus the radial distance from the heater at different times considering SSA = 44, and 150 m²/g, respectively. It is evident that in the case of SSA = 44 m²/g (and $c_{eq} = 10^{-7}$ M), the pore pressure diffusivity is stronger because the thermo-osmotic flow is in the same direction as Darcy's flow. However, for SSA = 150 m²/g, the direction of thermo-osmotic flow is in the opposite direction of Darcy's flow and is toward the heat source, thus higher PWP is predicted. SSA = 44 m²/g is chosen as the value for the specific surface area since, SSA = 150 m²/g yields unrealistically large thermo-osmotic conductivity (with the negative sign) and thus higher PWP as it is evident in Fig. 7(b) and (d), respectively. It should be also mentioned that SSA = 44 m²/g is suggested by Gonçalvès et al. (2012) for Boom clay. Romero et al. (2011) also used SSA = 53 m²/g that is close to the value we consider in the rest of this study. Fig. 7(e) and (f) show the effect of various bulk concentrations on

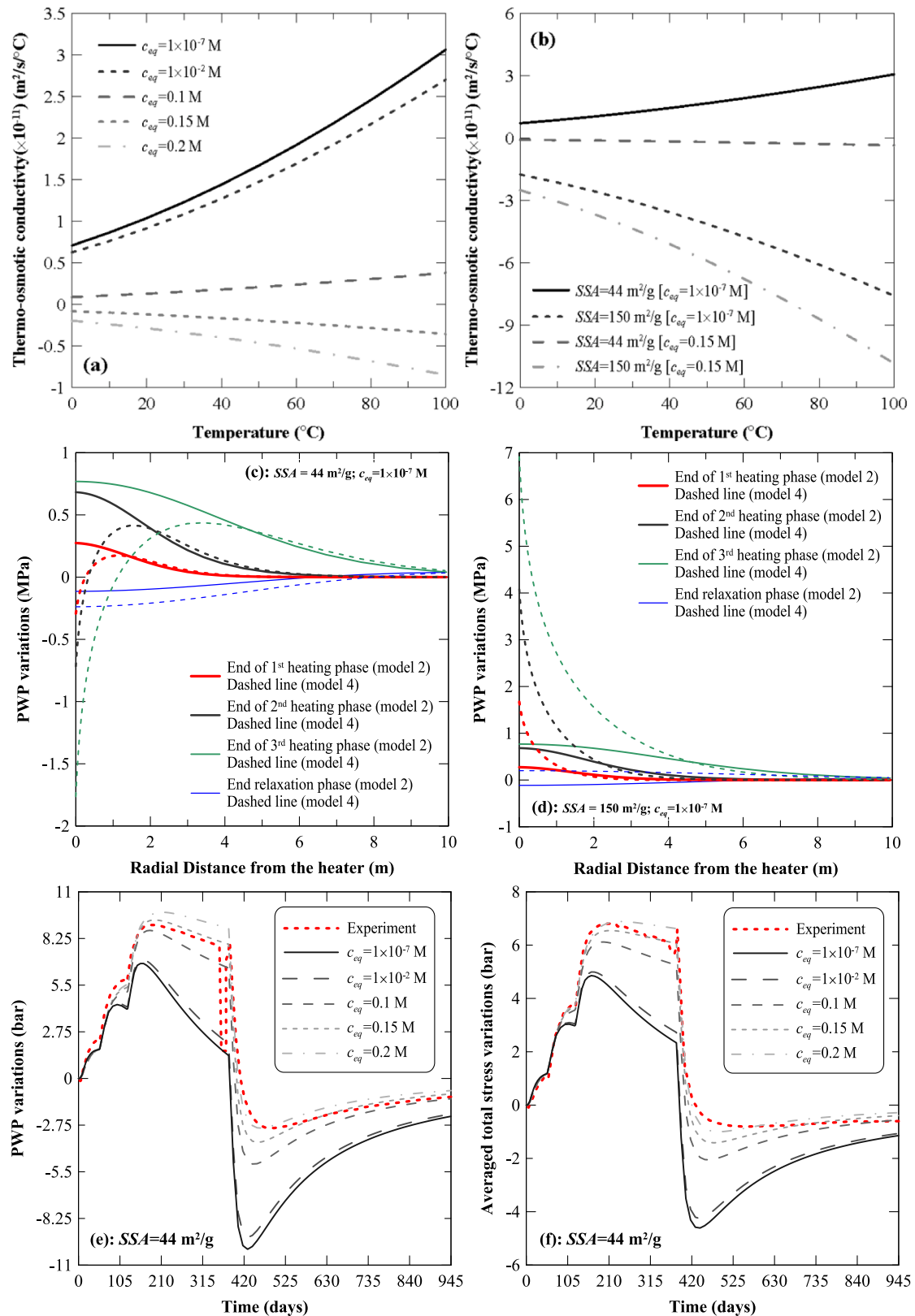


Fig. 7. (a) Thermo-osmotic conductivity against temperature for different c_{eq} , (b) thermo-osmotic conductivity against temperature for different SSA, (c) PWP variation based on models 2 and 4 along with the radial distance for SSA = 44 m²/g, (d) PWP variation based on models 2 and 4 along with the radial distance for SSA = 150 m²/g, (e) PWP variation based on model 4 against time for different c_{eq} , and (f) total stress variation based on model 4 against time for different c_{eq} .

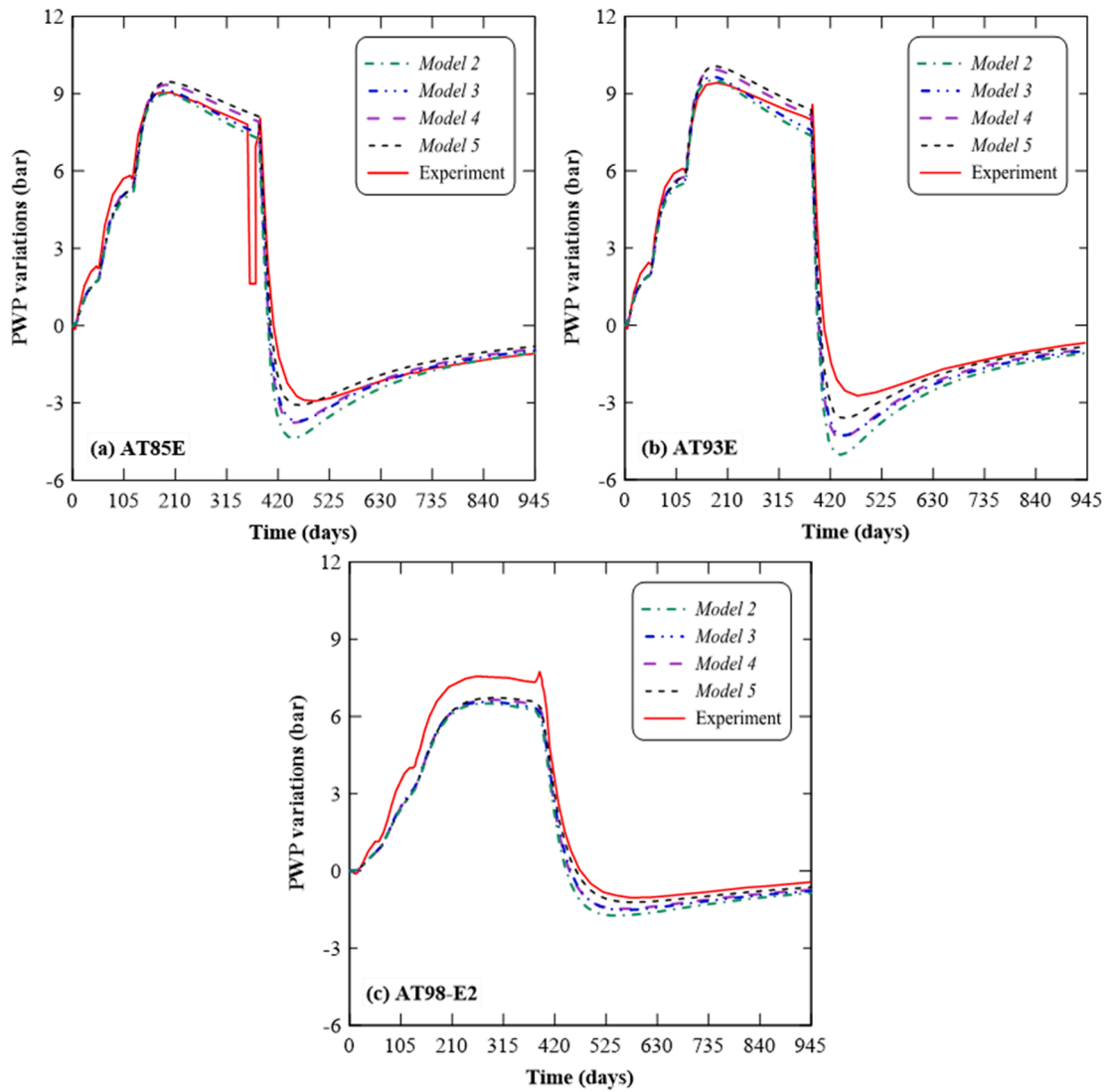


Fig. 8. Thermal pressurization against time by utilizing model 4 and 5: (a) $x = 1.5$ m, (b) $x = 1.3$ m, and (c) $x = 2.68$ m from the heat source (Models 2 and 3 are included for comparison).

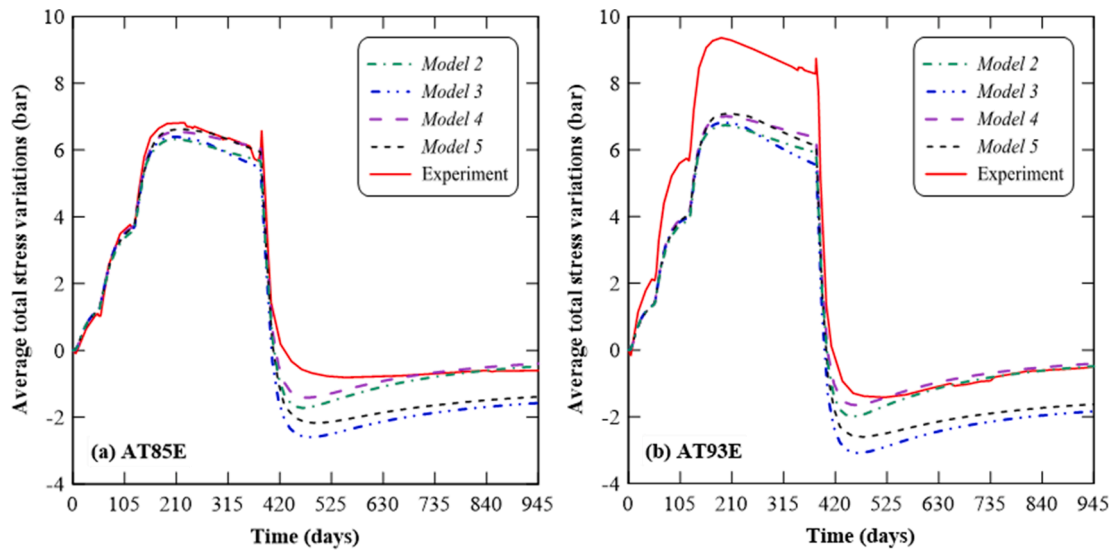


Fig. 9. Averaged total stress variations against time by utilizing model 4 and 5: (a) $x = 1.5$ m and (b) $x = 1.3$ m from the heat source (Models 2 and 3 are included for comparison).

the PWP and total stress variation at $x = 1.5$ m. It is noted that $c_{eq} = 10^{-7}$ M highly overestimates the PWP diffusion and, consequently, stress variations for thermo-osmotic flow. Comparison of the numerical results with the experimental observations demonstrates that $c_{eq} = 0.15$ M renders the best prediction for both PWP and total stress variation. Therefore, based on the results of the parametric study and suggested values in the literature, we consider $c_{eq} = 0.15$ M and $SSA = 44$ m²/g in this research.

3.5.5. Thermal pressurization (Models 4 and 5)

The predictions of thermal pressurization obtained from models 4 and 5 at three different measurement boreholes are illustrated in Fig. 8 (a)-(c) considering thermo-osmotic flow and thermal infiltration. Models 2 and 3 are also included to visualize the models' differences. In both models 4 and 5, the thermo-osmotic conductivity varies from $k_T/\mu = -8.24 \times 10^{-13}$ m²/C/s (for 0 °C) to -3.56×10^{-12} m²/C/s (for 100 °C). At all distances from the heater, model 4 (TPE model) shows a higher PWP variation in the negative pressurization regime compares to model 5 (TPEP mode) due to the difference in deformation characteristics of these models. Indeed, TPE assumes a more mechanically rigid porous structure which prevents the excessive changes of porous structure, and therefore, higher thermal pressurization. On the other hand, the TPEP model considering the ACMEG-T constitutive model yields a relatively more flexible structure which is induced by thermal softening. Regardless of the mechanical constitutive model, the thermo-osmotic flow seems to slightly improve the thermal pressurization estimation for all three measuring locations.

3.5.6. Total stress variations (Models 4 and 5)

The averaged total stress resulting from Models 4 and 5 for AT85E and AT93E are presented in Fig. 9(a) and (b), respectively, and compared with models 2 and 3. The overall agreement between simulations and experimental observations is obtained. However, it is evident that even the utilization of thermo-osmotic flow could not capture the measured experimental stress variations in Fig. 9(b). It is to be noted that 3D geometric models with consideration of anisotropic THM characteristics of Boom clay (or other anisotropic clays) may improve the result of the current study (Braun et al., 2021a; François et al., 2014); if we assume the experimental measurements were carefully calibrated for canceling the effect of temperature on the sensor's readings. Here, with consideration of a relatively simpler model (i.e., 2D axisymmetric condition with isotropic assumption) the effect of thermo-osmotic flow with variable thermo-osmotic conductivity and thermal infiltration are investigated by utilizing both thermo-poroelastic and thermo-

poroelastoplastic constitutive models. Reasonable results have been achieved which can be used as a benchmark for more sophisticated modeling approaches. It should be noted that in Figs. 8 and 9, thermo-osmosis effects are shown for distinct points away from the heat source. It is expected that thermo-osmosis effects would be more significant closer to the heat source where higher temperature variations occur.

3.5.7. Variations of thermal pressurization and total stress in the radial distance

The variations of total stress and PWP along the radial distance from the heater are shown, respectively, in Fig. 10(a) and (b). Fig. 10(a) solely interpret the effect of thermo-plastic deformation on the THM process in Boom clay and expresses that the variations of total stress obtained from the thermo-poroelastoplastic model (model 3) are lower than the thermo-poroelastic one (model 2) in the heating phase, while it is higher than model 2 at the end of the cooling phase. The difference in the numerical results obtained from these two models is evident at the elevated temperatures (e.g., at the end of 3rd heating phase) and grows in a larger area farther from the heater following the growth of thermal deformation in the vicinity of the heater. As it was mentioned earlier, the difference between the results obtained from TPE and TPEP models (Model 2 and 3) is more obvious closer to the heat source. Both models indicate that the influential zone for total stress variation goes beyond $x = 5$ m from the heater.

In Fig. 10(b) the effect of thermo-osmotic flow on the hydro-mechanical process is investigated using the TPE model. Thermo-osmotic flow has a reverse effect on the diffusion of thermal pressurization. That is why higher thermal pressurization is obtained during the heating phase in model 4 compares to model 2 in which thermo-osmosis and thermal infiltration are neglected. The influence of thermo-osmotic flow on thermal pressurization is less pronounced in the cooling step due to the existence of a lower thermal gradient in the medium.

The non-Darcian fluid flux (both Darcy's and thermo-osmotic flow) is schematically visualized in Fig. 11(a) and (b) at the end of heating and cooling phases close to the heater by considering model 4. PWP variations are also shown in the colored contours. In the heating phase, Darcy's flow and thermo-osmotic flow are in opposite directions (Fig. 11 (a)). The heat emits from the heater and propagates to the surrounding soil and pressurizes the fluid. Therefore, the pressurized fluid diffuses further into the soil as well, which explains the direction of Darcy's flow. However, because of the negative value of thermo-osmotic conductivity obtained in this study, thermo-osmotic flow is towards the elevated temperature region (i.e., towards the heater). In Fig. 11(b), where the

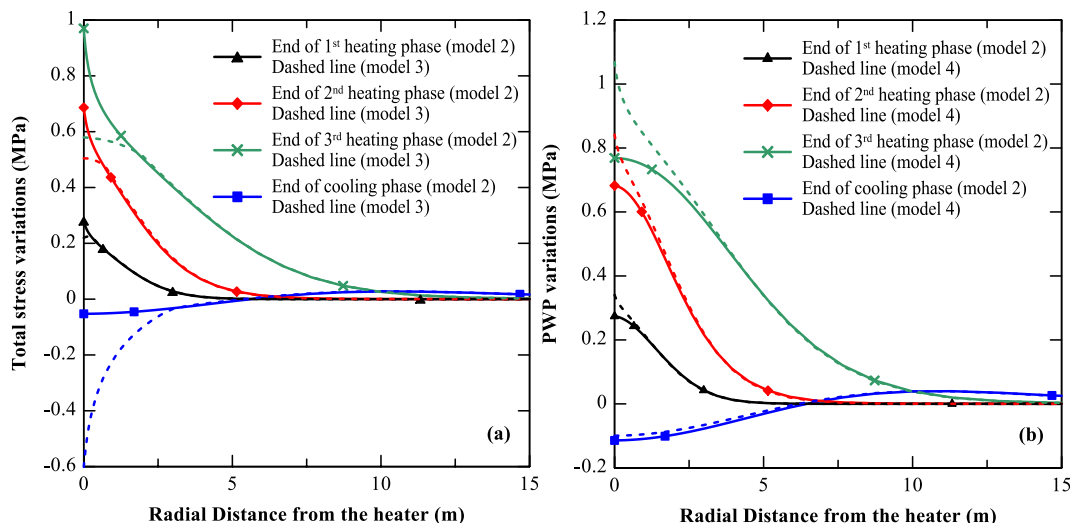


Fig. 10. Variations of total stress [(a)] and PWP [(b)] along with the radial distance from the heater (comparison of models 2, 3, and 4).

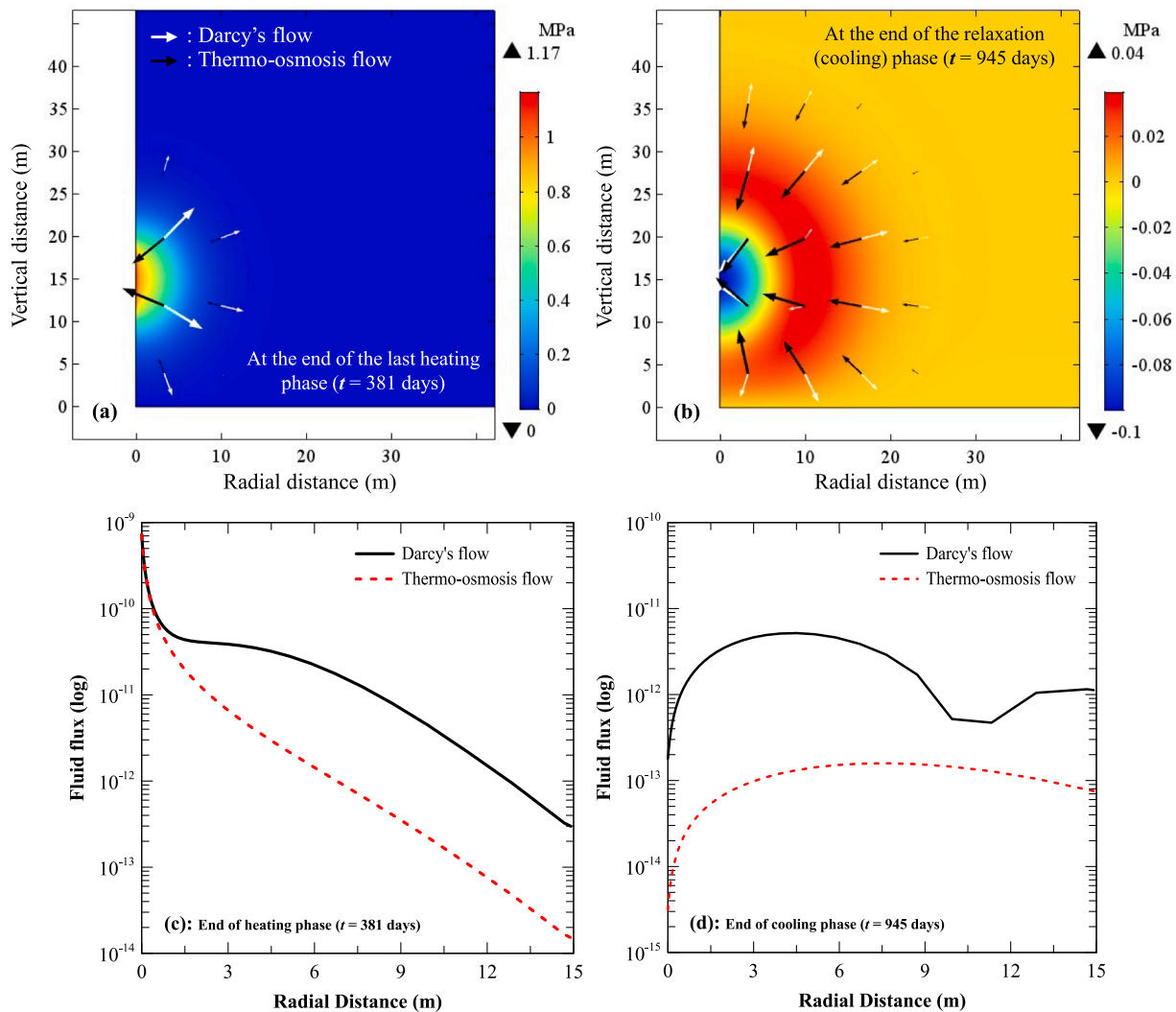


Fig. 11. Fluid flux representation in the vicinity of the heater. The white and black arrows show the velocity field and the direction of the flow governed by Darcy's flow and thermo-osmotic flow, respectively. (a) and (c) at $t = 381$ days (end of heating phase), (b) and (d) $t = 945$ days (end of cooling phase).

heater is already turned off for some time, Darcy's flow, close to the heater, is towards the heater, while in farther distance, it is still propagating (same direction as in the heating phase). This observation is because the thermal pressurization ($p_f - p_{f0}$) drops to a negative value in about a 6 m radius from the heater, while still yields a positive value approximately from 6 to 25 m. On the other hand, the thermo-osmotic flow is steadily towards the heater and oppositely follows the thermal diffusion in the medium since the temperature variations are positive during the heating phase and even at the end of the cooling phase ($T - T_0$). Please note in the case with different c_{eq} and SSA the thermo-osmotic conductivity might be a positive value and therefore thermo-osmotic flow should be in the same direction as the thermal diffusion during the heating phase or farther from the heat source during the cooling phase.

3.5.8. Non-Darcian fluid flux in the radial distance

Fig. 11(c) and (d) illustrate the magnitude of Darcy's flow and thermo-osmotic flow at the end of the heating and cooling phases, respectively. It is interesting to report that, at the end of the heating phase, thermo-osmotic flow is in the same order as Darcy's flow close to the heater; however, in the cooling phase when a thermal gradient is lower, the magnitude of the thermo-osmotic flow is negligible in comparison to Darcy's flow. The comparison in Fig. 11(a)-(d) confirm the importance of the thermo-osmosis phenomenon locally close to the heat

sources embedded in clayey soils. It should be mentioned that numerical results which are not reported in this figure illustrate that thermal infiltration has a negligible effect on the THM response of Boom clay compares to the thermo-osmosis phenomenon in this study.

3.5.9. Volumetric deformation of the soil

Fig. 12(a)-(d) exhibit the evolution elastic, plastic, thermal, and total volumetric strain, respectively, at different distances for 945 days (2.5 years). Note that positive values show contraction and negative values express expansion. In the heating phase, the pressurized fluid decreases the effective stress, and thus dilates the pores and causes reversible expansion which is depicted in Fig. 12(a). After the heater is turned off, the sudden reduction in thermally induced pore water pressure (due to lower thermal gradient) increases the effective stress in the soil, and consequently, contract the soil. PWP dissipation starts as early as the thermal loading initiates, however at the first two stages of the heating the generation of thermally induced excess pore water pressure is more than the dissipation rate and thus thermal expansion is dominated for the first 110 days. Nonetheless, during the third phase of the heating, dissipation of the thermally induced pore water pressure, and consequently, contraction occurs in this period despite the heater is still on. At the end of the second year (end of the experiment) and in the vicinity of the heater, negative PWP is dissipated; therefore, the effective stress is decreased, and elastic dilation takes place for the second time. Fig. 12(b)

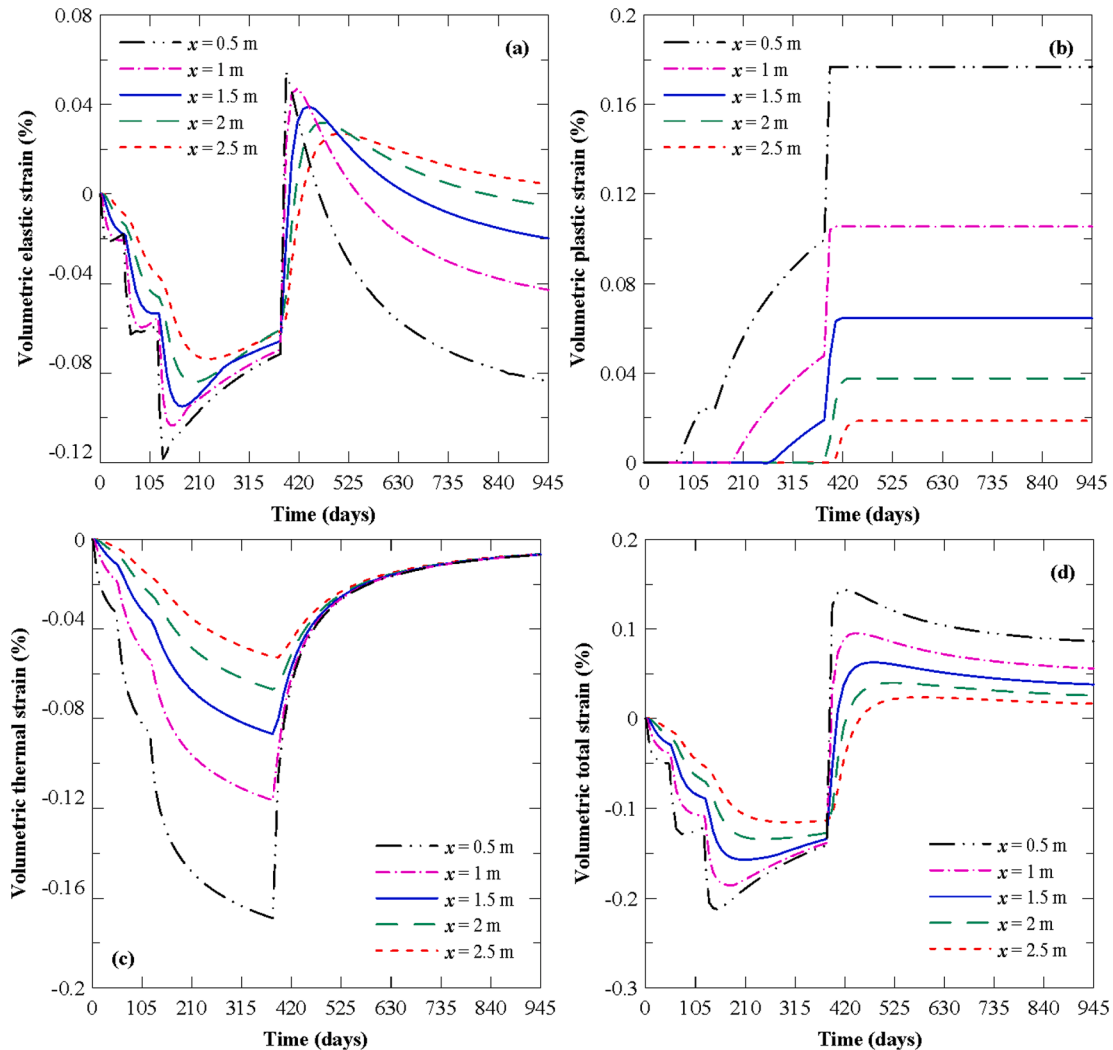


Fig. 12. (a) volumetric elastic strain, (b) volumetric plastic strain, (c) volumetric thermal strain, and (d) volumetric total strain variations against time from model 3.

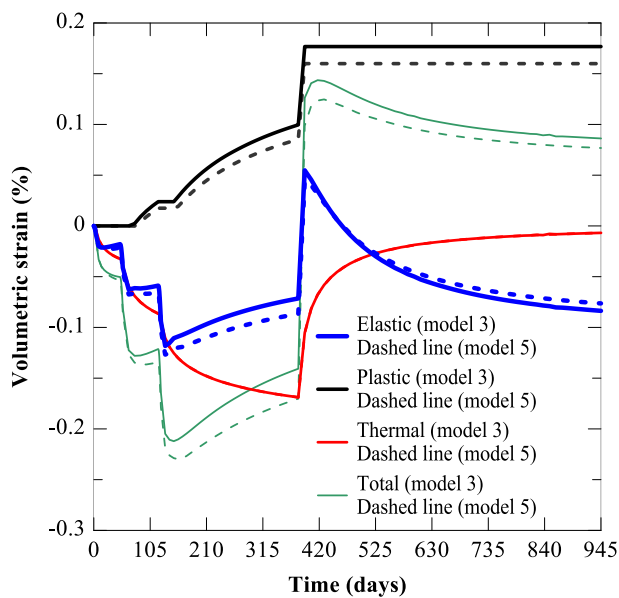


Fig. 13. The effect of osmotic flow on the thermo-mechanical deformation characteristics of Boom clay against time (at x = 0.5 m).

demonstrates that plastic deformation occurs and evolves from the beginning of the first heating phase and reaches its maximum value at the end of the second heating phase where it remains constant thereafter the cooling phase for all the locations shown in the figure. The irrecoverable contractive plastic strain has an additional effect on lowering the effective stress as well (by decreasing the mechanical strength of the material). The sudden jump of the volumetric plastic strain at the beginning of the cooling phase is related to the rapid increase in the preconsolidation pressure (thermal hardening) which happens due to the cooling effect which can be interpreted as thermal volume reduction (thermal consolidation) after a heating/cooling cycle. The significance of thermal strain on the THM process is shown to be in the heating phase and it slowly fades away when temperature drops after the heater is turned off (Fig. 12(c)). The contribution of each strain (elastic, plastic, and thermal strain) in total strain is presented in Fig. 12(d). Thermo-elastic deformation is dominant in the heating phases, where in the cooling phase the plastic deformation (manifested as thermal consolidation) has a major role close to the heater.

3.5.10. Effect of thermo-osmosis flow on volumetric deformation of the soil

The effect of thermo-osmotic flow on thermo-mechanical deformation of the soil is presented in Fig. 13. Thermo-osmotic flow does not have any impact on thermal strain (heat transfer mechanics and thermal response). On the other hand, thermo-osmotic flow increases the evolution of elastic strain yet decreases the plastic strain by changing the

thermal pressurization (PWP). Thermo-osmotic flow increases the thermal pressurization; therefore, results in higher elastic dilation during the heating phases (evident from the beginning of the 2nd stage of heating onward) while it has a negligible effect on elastic strain during the cooling phases when the soil thermal gradient is low. On the other hand, the thermo-osmosis phenomenon reduces the effective stress that affects the plastic strain in both heating and cooling phases. As it can be observed from Fig. 13, during the heating phase, the total strain follows the same trend as elastic strain, and in the cooling phase, the total strain follows the plastic deformation. Comparison of total strain with and without considering the thermo-osmosis phenomenon indicates the importance of thermo-osmotic flow in the second and third stages of the heating and cooling phases.

4. Conclusion

In this study, a series of numerical simulations are conducted to shed a light on the effects of different thermal, hydraulic, and mechanical properties of the medium and the saturating fluid on the THM process of Boom clay. We also analyze the effect of the thermo-osmosis phenomenon and thermal infiltration on the THM process in clayey soils. Therefore, five different models for different thermal, hydraulic, and mechanical constitutive models are presented. For a complete description of the THM process, careful examination of different temperature-dependent properties of the fluid and medium are also considered. Moreover, thermo-osmotic flow is incorporated as an additional diffusion term which serves as the direct coupling effect of temperature field on fluid mass balance equation (strong coupling). A thorough comparison of each element on thermal pore pressurization, total stress, and temperature field is presented by comparing the numerical THM analysis with experimental observations of Boom clay in the ATLAS III test. All models yield reasonable results during heating phases except model 1 which considers constant thermo-hydraulic properties of water and overestimates the thermal pressurization. It is found that the thermal properties of water such as the thermal expansion coefficient of the bulk water play an important role in thermal pressurization and mechanical deformation of the medium. The plastic deformation and thermal infiltration have limited effects on the temperature field in our study. The thermo-osmosis phenomenon may reduce or excite the thermal pressurization magnitude and facilitate the fluid flow depending on the positivity or negativity of the thermo-osmotic conductivity. The parametric study on the different specific surface area (SSA) and bulk salt concentration of water, and validating it with experimental observations, suggests that the thermo-osmotic conductivity should be negative in Boom clay. The results determine that thermo-osmotic flow is needed to accurately analyze the THM process close to heat sources. While thermal infiltration has a negligible effect on the THM response of Boom clay considered in this study. Additionally, it is shown that the inclusion of thermo-plastic deformation is significant during the cooling phase when the negative variations of pore water pressure are generated. In general, the thermal softening during the heating phase and thermal hardening during the cooling phase change the stress distribution and material characteristics.

CRedit authorship contribution statement

Mohammadreza Mir Tamizdoust: Resources, Conceptualization, Methodology, Software, Formal analysis, Investigation, Data curation, Writing – original draft, Writing – review & editing. **Omid Ghasemi-Fare:** Project administration, Conceptualization, Methodology, Supervision, Data curation, Funding acquisition, Writing – original draft, Writing – review & editing.

Declaration of Competing Interest

The authors declare that they have no known competing financial

interests or personal relationships that could have appeared to influence the work reported in this paper.

Acknowledgments

The authors would also like to gratefully acknowledge the financial support by the National Science Foundation under Grant No. CMMI-1804822.

References

- Abed, A.A., Solowski, W.T., 2017. A study on how to couple thermo-hydro-mechanical behaviour of unsaturated soils: Physical equations, numerical implementation and examples. *Comput. Geotech.* 92, 132–155.
- Abuel-Naga, H.M., Bergado, D.T., Ramana, G.V., Grino, L., Rujivipat, P., Thet, Y., 2006. Experimental evaluation of engineering behavior of soft Bangkok clay under elevated temperature. *J. Geotech. Geoenviron. Eng.* 132 (7), 902–910.
- Abuel-Naga, H.M., Bergado, D.T., Bouazza, A., Ramana, G.V., 2007a. Volume change behaviour of saturated clays under drained heating conditions: experimental results and constitutive modeling. *Can. Geotech. J.* 44 (8), 942–956.
- Abuel-Naga, H.M., Bergado, D.T., Bouazza, A., 2007b. Thermally induced volume change and excess pore water pressure of soft Bangkok clay. *Eng. Geol.* 89 (1–2), 144–154.
- Ai, Z.Y., Wang, L.J., 2015. Axisymmetric thermal consolidation of multilayered porous thermoelastic media due to a heat source. *Int. J. Numer. Anal. Meth. Geomech.* 39 (17), 1912–1931.
- Al-Mukhtar, M., Belanteur, N., Tessier, D., Vanapalli, S.K., 1996. The fabric of a clay soil under controlled mechanical and hydraulic stress states. *Appl. Clay Sci.* 11 (2–4), 99–115.
- Baldi, G., Borsetto, M., Hueckel, T.J.L.C.o.t.E.C., 1987. Calibration of mathematical models for simulation of the thermal, seepage and mechanical behaviour of Boom clay: Final report, EUR 10924 EN.
- Baldi, G., Hueckel, T., Peano, A., Pellegrini, R., 1991. Developments in modelling of thermo-hydro-geomechanical behaviour of boom clay and clay-based buffer materials. Commission of the European Communities. Nuclear science and technology.
- Baldi, G., Hueckel, T., Pellegrini, R., 1988. Thermal volume changes of the mineral–water system in low-porosity clay soils. *Can. Geotech. J.* 25 (4), 807–825.
- Ballarini, E., Graupner, B., Bauer, S., 2017. Thermal-hydraulic-mechanical behavior of bentonite and sand-bentonite materials as seal for a nuclear waste repository: Numerical simulation of column experiments. *Appl. Clay Sci.* 135, 289–299.
- Bernier, F., Li, X.L., Bastiaens, W., 2007. Twenty-five years' geotechnical observation and testing in the Tertiary Boom Clay formation. *Géotechnique* 57 (2), 229–237.
- Braun, P., Ghabezloo, S., Delage, P., Sulem, J., Conil, N., 2021a. Transversely Isotropic Poroelastic Behaviour of the Callovo-Oxfordian Claystone: A Set of Stress-Dependent Parameters. *Rock Mech. Rock Eng.* 54 (1), 377–396.
- Braun, P., Ghabezloo, S., Delage, P., Sulem, J., Conil, N., 2021b. Thermo-poro-elastic behaviour of a transversely isotropic shale: Thermal expansion and pressurization. *Rock Mech. Rock Eng.* 54 (1), 359–375.
- Chalindar, S., Charlier, R., Collin, F., Dizier, A., François, B., Fokkens, J., Garitte, B., Gens, A., Chen, G., Hart, J., 2010. Thermal impact on the damaged zone around a radioactive waste disposal in clay host rocks, deliverable 13: In situ heating test ATLAS in Mol. TIMODAZ project. EUROPEAN COMMISSION.
- Chaudhry, A.A., Buchwald, J., Nagel, T., 2021. Local and global spatio-temporal sensitivity analysis of thermal consolidation around a point heat source. *Int. J. Rock Mech. Min. Sci.* 139, 104662. <https://doi.org/10.1016/j.ijrmms.2021.104662>.
- Chen, G., Dizier, A., Li, X., Verstricht, J., Sillen, X., Levasseur, S., 2021a. Numerical Prediction of the Large-Scale In Situ PRACTLAY Heater Test in the Boom Clay. *Rock Mech. Rock Eng.* 54 (5), 2197–2218.
- Chen, G.J., Sillen, X., Verstricht, J., Li, X.L., 2011. ATLAS III in situ heating test in boom clay: Field data, observation and interpretation. *Comput. Geotech.* 38 (5), 683–696.
- Chen, W.Q., Sedighi, M., Jivkov, A.P., 2021b. Thermo-osmosis in hydrophilic nanochannels: mechanism and size effect. *Nanoscale* 13 (3), 1696–1716.
- Chen, W.Z., Ma, Y.S., Yu, H.D., Li, F.F., Li, X.L., Sillen, X., 2017. Effects of temperature and thermally-induced microstructure change on hydraulic conductivity of Boom Clay. *J. Rock Mech. Geotech. Eng.* 9 (3), 383–395.
- Cherati, D.Y., Ghasemi-Fare, O., 2021. Unsaturated thermal consolidation around a heat source. *Comput. Geotech.* 134, 104091. <https://doi.org/10.1016/j.compgeo.2021.104091>.
- Coussy, O., 2004. *Poromechanics*. John Wiley & Sons.
- Cui, W., Potts, D.M., Zdravković, L., Gawęcka, K.A., Taborda, D.M.G., 2018. An alternative coupled thermo-hydro-mechanical finite element formulation for fully saturated soils. *Comput. Geotech.* 94, 22–30.
- Cui, Y.J., Sultan, N., Delage, P., 2000. A thermomechanical model for saturated clays. *Can. Geotech. J.* 37 (3), 607–620.
- Dafalias, Y.F., 1981. The concept and application of the bounding surface in plasticity theory. In: Hult, J., Lemaitre, J. (Eds.), *Physical Non-Linearities in Structural Analysis*. Springer Berlin Heidelberg, Berlin, Heidelberg, pp. 56–63. https://doi.org/10.1007/978-3-642-81582-9_9.
- Delage, P., Sultan, N., Cui, Y.J., 2000. On the thermal consolidation of Boom clay. *Can. Geotech. J.* 37 (2), 343–354.
- Delaney, P.T., 1982. Rapid intrusion of magma into wet rock: groundwater flow due to pore pressure increases. *J. Geophys. Res. Solid Earth* 87, 7739–7756.

- Derjaguin, B., Sidorenkov, G., 1941. On thermo-osmosis of liquid in porous glass. *CR Acad. Sci. URSS* 32, 622–626.
- François, B., Labrousse, V., Dizier, A., Marinelli, F., Charlier, R., Collin, F., 2014. Hollow cylinder tests on boom clay: Modelling of strain localization in the anisotropic excavation damaged zone. *Rock Mech. Rock Eng.* 47 (1), 71–86.
- François, B., Laloui, L., Laurent, C., 2009. Thermo-hydro-mechanical simulation of ATLAS in situ large scale test in Boom Clay. *Comput. Geotech.* 36 (4), 626–640.
- Gens, A., Vaunat, J., Garitte, B., Wileveau, Y., 2007. In situ behaviour of a stiff layered clay subject to thermal loading: observations and interpretation. *Géotechnique* 57 (2), 207–228.
- Ghabezloo, S., Sulem, J., 2009. Stress dependent thermal pressurization of a fluid-saturated rock. *Rock Mech. Rock Eng.* 42 (1), 1–24.
- Ghabezloo, S., Sulem, J., 2010. Temperature induced pore fluid pressurization in geomaterials. *arXiv preprint arXiv:1011.6501*.
- Gonçalves, J., de Marsily, G., Tremosa, J., 2012. Importance of thermo-osmosis for fluid flow and transport in clay formations hosting a nuclear waste repository. *Earth Planet. Sci. Lett.* 339–340, 1–10.
- Gonçalves, J., Trémosa, J., 2010. Estimating thermo-osmotic coefficients in clay-rocks: I. Theoretical insights. *J. Colloid Interface Sci.* 342 (1), 166–174.
- Gonçalves, J., Violette, S., Wendling, J., 2004. Analytical and numerical solutions for alternative overpressuring processes: Application to the Callovo-Oxfordian sedimentary sequence in the Paris basin, France. *Journal of Geophysical Research: Solid Earth* 109 (B2). <https://doi.org/10.1029/2002JB002278>.
- Gray, D.H., 1966. Coupled flow phenomena in clay-water systems.
- Guayacán-Carrillo, L.-M., Ghabezloo, S., Sulem, J., Seyedi, D.M., Armand, G., 2017. Effect of anisotropy and hydro-mechanical couplings on pore pressure evolution during tunnel excavation in low-permeability ground. *Int. J. Rock Mech. Min. Sci.* 97, 1–14.
- Hueckel, T., Borsetto, M., 1990. Thermoplasticity of saturated soils and shales: constitutive equations. *J. Geotechnical Eng.* 116 (12), 1765–1777.
- Hueckel, T., François, B., Laloui, L., 2011. Temperature-dependent internal friction of clay in a cylindrical heat source problem. *Géotechnique* 61 (10), 831–844.
- Hueckel, T., Pellegrini, R., 1992. Effective stress and water pressure in saturated clays during heating-cooling cycles. *Can. Geotech. J.* 29 (6), 1095–1102.
- Joshaghani, M., Ghasemi-Fare, O., 2019. A Study on thermal consolidation of fine grained soils using modified triaxial cell, Eighth International Conference on Case Histories in Geotechnical Engineering. ASCE, Philadelphia, Pennsylvania, pp. 148–156.
- Joshaghani, M., Ghasemi-Fare, O., 2021. Exploring the effects of temperature on intrinsic permeability and void ratio alteration through temperature-controlled experiments. *Eng. Geol.* 293, 106299. <https://doi.org/10.1016/j.enggeo.2021.106299>.
- Laloui, L., 1993. Modélisation du comportement thermo-hydro-mécanique des milieux poreux anélastiques. Ecole Centrale Paris.
- Laloui, L., Cekeravac, C., 2003. Thermo-plasticity of clays: an isotropic yield mechanism. *Comput. Geotech.* 30 (8), 649–660.
- Laloui, L., François, B., 2009. ACMEGT: soil thermoplasticity model. *J. Eng. Mech.* 135 (9), 932–944.
- Malekzadeh, F.A., Pak, A., 2009. A discretized analytical solution for fully coupled non-linear simulation of heat and mass transfer in poroelastic unsaturated media. *Int. J. Numer. Anal. Meth. Geomech.* 33 (13), 1589–1611.
- McTigue, D.F., 1986. Thermoelastic response of fluid-saturated porous rock. *J. Geophys. Res. Solid Earth* 91 (B9), 9533. <https://doi.org/10.1029/JB091iB09p09533>.
- Mertens, J., Bastiaens, W., Dehandschutter, B., 2004. Characterisation of induced discontinuities in the Boom Clay around the underground excavations (URF, Mol, Belgium). *Appl. Clay Sci.* 26 (1–4), 413–428.
- Modaressi, H., Laloui, L., 1997. A thermo-viscoplastic constitutive model for clays. *Int. J. Numer. Anal. Meth. Geomech.* 21 (5), 313–335.
- Niu, J., Wang, X., Gong, S., Ling, D., 2020. Exact Solutions for Investigating Thermal Response of Saturated Soil Induced by Temperature Change. *Int. J. Geomech.* 20 (10), 04020177. [https://doi.org/10.1061/\(ASCE\)GM.1943-5622.0001803](https://doi.org/10.1061/(ASCE)GM.1943-5622.0001803).
- Plúa, C., Vu, M.N., Armand, G., Rutqvist, J., Birkholzer, J., Xu, H., Guo, R., Thatcher, K. E., Bond, A.E., Wang, W., Nagel, T., Shao, H., Kolditz, O., 2021. A reliable numerical analysis for large-scale modelling of a high-level radioactive waste repository in the Callovo-Oxfordian claystone. *Int. J. Rock Mech. Min. Sci.* 140, 104574. <https://doi.org/10.1016/j.ijrmm.2020.104574>.
- Potts, D.M., Cui, W., Zdravković, L., 2021. A coupled THM finite element formulation for unsaturated soils and a strategy for its nonlinear solution. *Comput. Geotech.* 136, 104221. <https://doi.org/10.1016/j.compgeo.2021.104221>.
- Revil, A., 2017a. Transport of water and ions in partially water-saturated porous media. Part 1. Constitutive equations. *Adv. Water Resources* 103, 119–138.
- Revil, A., 2017b. Transport of water and ions in partially water-saturated porous media. Part 2. Filtration effects. *Advances in Water Resources* 103, 139–152.
- Revil, A., Leroy, P., 2004. Constitutive equations for ionic transport in porous shales. *Journal of Geophysical Research: Solid Earth* 109.
- Rice, J.R., 2006. Heating and weakening of faults during earthquake slip. *Journal of Geophysical Research: Solid Earth* 111 (B5), n/a–n/a.
- Romero, E., Della vecchia, G., Jommi, C., 2011. An insight into the water retention properties of compacted clayey soils. *Géotechnique* 61 (4), 313–328.
- Roshan, H., Andersen, M.S., Acworth, R.L., 2015. Effect of solid–fluid thermal expansion on thermo-osmotic tests: an experimental and analytical study. *J. Petrol. Sci. Eng.* 126, 222–230.
- Rutqvist, J., Barr, D., Datta, R., Gens, A., Millard, A., Olivella, S., Tsang, C.-F., Tsang, Y., 2005. Coupled thermal–hydrological–mechanical analyses of the Yucca Mountain Drift Scale Test—Comparison of field measurements to predictions of four different numerical models. *Int. J. Rock Mech. Min. Sci.* 42 (5–6), 680–697.
- Sánchez, M., Gens, A., do Nascimento Guimarães, L., Olivella, S., 2005. A double structure generalized plasticity model for expansive materials. *Int. J. Numer. Anal. Meth. Geomech.* 29 (8), 751–787.
- Sánchez, M., Gens, A., Olivella, S., 2010. Effect of thermo-coupled processes on the behaviour of a clay barrier submitted to heating and hydration. *Anais da Academia Brasileira de Ciências* 82 (1), 153–168.
- Sánchez, M., Gens, A., Olivella, S., 2012. THM analysis of a large-scale heating test incorporating material fabric changes. *Int. J. Numer. Anal. Meth. Geomech.* 36 (4), 391–421.
- Sánchez, M., Gens, A., Villar, M.V., Olivella, S., 2016. Fully coupled thermo-hydro-mechanical double-porosity formulation for unsaturated soils. *Int. J. Geomech.* 16, D4016015.
- Schuster, K., Alheid, H., Eichhorn, P., Boddener, D., 2001. In situ seismic in the new shaft at the underground research facility Mol/Belgium. Final report 9Y3212010000, BGR, Hannover.
- Shackelford, C.D., Lu, N., Malusis, M.A., Sample-Lord, K.M., 2019. Research challenges involving coupled flows in geotechnical engineering. *Geotechnical Fundamentals for Addressing New World Challenges*. Springer 237–274.
- Spang, B., 2002. Excel add-in for properties of water and steam in SI-units. *Water97_v13.xla*. Hamburg.
- Tamizdoust, M.M., Ghasemi-Fare, O., 2019. Numerical Analysis on Feasibility of Thermally Induced Pore Fluid Flow in Saturated Soils, Eighth International Conference on Case Histories in Geotechnical Engineering. ASCE, Philadelphia, Pennsylvania, pp. 73–82.
- Tamizdoust, M.M., Ghasemi-Fare, O., 2020a. Comparison of thermo-poroelastic and thermo-poroelastoplastic constitutive models to analyze THM process in clays, E3S Web of Conferences 205, 04008. <https://doi.org/10.1051/e3sconf/202020504008>.
- Tamizdoust, M.M., Ghasemi-Fare, O., 2020b. Coupled thermo-hydro-mechanical modeling of saturated Boom clay, Geo-Congress 2020: Geo-Systems, Sustainability, Geoenvironmental Engineering, and Unsaturated Soil Mechanics. American Society of Civil Engineers Reston, VA, pp. 340–348.
- Tamizdoust, M.M., Ghasemi-Fare, O., 2020c. A fully coupled thermo-poro-mechanical finite element analysis to predict the thermal pressurization and thermally induced pore fluid flow in soil media. *Comput. Geotech.* 117, 103250. <https://doi.org/10.1016/j.compgeo.2019.103250>.
- Tamizdoust, M.M., Ghasemi-Fare, O., 2022. Long-term Thermo-hydraulic Response of the Shallow Subsurface soil in the Vicinity of a Buried Horizontal Heat Source. *Int. J. Heat Mass Transf.* 183, 122120. <https://doi.org/10.1016/j.ijheatmasstransfer.2021.122120>.
- Tremosa, J., Gonçalves, J., Matray, J.-M., 2012. Natural conditions for more limited osmotic anisothermal fluid pressures in sedimentary basins. *Water Resour. Res.* 48 (4) <https://doi.org/10.1029/2011WR010914>.
- Tsang, C.F., Barnichon, J.D., Birkholzer, J., Li, X.L., Liu, H.H., Sillen, X., 2012. Coupled thermo-hydro-mechanical processes in the near field of a high-level radioactive waste repository in clay formations. *Int. J. Rock Mech. Min. Sci.* 49, 31–44.
- Veiskarami, M., Tamizdoust, M.M., 2017. Bifurcation analysis in sands under true triaxial conditions with coaxial and noncoaxial plastic flow rules. *J. Eng. Mech.* 143 (10), 04017120. [https://doi.org/10.1061/\(ASCE\)EM.1943-7889.0001344](https://doi.org/10.1061/(ASCE)EM.1943-7889.0001344).
- Zagorščak, R., Sedighi, M., Thomas, H.R., 2017. Effects of thermo-osmosis on hydraulic behavior of saturated clays. *Int. J. Geomech.* 17 (3), 04016068. [https://doi.org/10.1061/\(ASCE\)GM.1943-5622.0000742](https://doi.org/10.1061/(ASCE)GM.1943-5622.0000742).
- Zeinali, S.M., Abdelaziz, S.L., 2021. Thermal Consolidation Theory. *J. Geotech. Geoenviron. Eng.* 147 (1), 04020147. [https://doi.org/10.1061/\(ASCE\)GT.1943-5606.0002423](https://doi.org/10.1061/(ASCE)GT.1943-5606.0002423).
- Zhai, X., Atefi-Monfared, K., 2020a. Explanation of early failure in porous media confined with flexible layers, considering thermo-osmosis, thermal-filtration and heat sink from fluid dilation. *Comput. Geotech.* 122, 103501. <https://doi.org/10.1016/j.compgeo.2020.103501>.
- Zhai, X., Atefi-Monfared, K., 2020b. Local thermal non-equilibrium effects on thermal pressurization in saturated porous media considering thermo-osmosis and thermal-filtration. *Comput. Geotech.* 126, 103729. <https://doi.org/10.1016/j.compgeo.2020.103729>.
- Zhai, X., Atefi-Monfared, K., 2020c. Thermo-poroelasticity under constant fluid flux and localized heat source. *Int. J. Heat Mass Transf.* 150, 119278. <https://doi.org/10.1016/j.ijheatmasstransfer.2019.119278>.
- Zhu, B., Ye, Z., Wang, L., Xu, W., Kong, D., Nagel, T., Kolditz, O., Chen, Y., 2021. Theoretical Investigation into Thermo-Osmosis and Thermofiltration Effects on Hydromechanical Behavior of Saturated Soils. *J. Eng. Mech.* 147 (4), 04021005. [https://doi.org/10.1061/\(ASCE\)EM.1943-7889.0001905](https://doi.org/10.1061/(ASCE)EM.1943-7889.0001905).